Near-Infrared Variability Study of the Central 2.3′×2.3′ of the Galactic Centre I. Catalog of Variable Sources

Hui Dong[1], Rainer Schödel[1], Benjamin F. Williams[2], Francisco Nogueras-Lara[1], Eulalia Gallego-Cano[1],Teresa Gallego-Calvente[1], Q. Daniel Wang[3], Mark R. Morris[4], Tuan Do[4], Andrea Ghez[4]

[1] *Instituto de Astrofísica de Andalucía (CSIC), Glorieta de la Astronomía S/N, E-18008 Granada, Spain*

[2] *Department of Astronomy, Box 351580, University of Washington, Seattle, WA 98195, USA*

[3] *Department of Astronomy, University of Massachusetts, Amherst, MA, 01003, USA*

[4]*Department of Physics and Astronomy, University of California, Los Angeles, CA, 90095, USA*

E-mail: hdong@iaa.es

ABSTRACT

We used four-year baseline *HST*/WFC3 IR observations of the Galactic Centre in the F153M band (1.53 μm) to identify variable stars in the central $\sim$2.3′×2.3′ field. We classified 3845 long-term (periods from months to years) and 76 short-term (periods of a few days or less) variables among a total sample of 33070 stars. For 36 of the latter ones, we also derived their periods (<3 days). Our catalog not only confirms bright long period variables and massive eclipsing binaries identified in previous works, but also contains many newly recognized dim variable stars. For example, we found δ Scuti and RR Lyrae stars towards the Galactic Centre for the first time, as well as one BL Her star (period < 1.3 d). We cross-correlated our catalog with previous spectroscopic studies and found that 319 variables have well-defined stellar types, such as Wolf-Rayet, OB main sequence, supergiants and asymptotic giant branch stars. We used colours and magnitudes to infer the probable variable types for those stars without accurately measured periods or spectroscopic information. We conclude that the majority of unclassified variables could potentially be eclipsing/ellipsoidal binaries and Type II Cepheids. Our source catalog will be valuable for future studies aimed at constraining the distance, star formation history and massive binary fraction of the Milky Way nuclear star cluster.

1. Introduction

The Galactic Centre (GC) contains a massive black hole (MBH), Sgr A* (4×10^6 $M_\odot$) and is located at a distance of only ∼8 kpc (Ghez et al. 2008; Gillessen et al. 2009; Chatzopoulos et al. 2015; Boehle et al. 2016), 100 times closer than the nearest nucleus of a comparable system, the Andromeda galaxy. Because of its proximity, the GC provides us with a unique lab to study the interaction between a MBH and its environment. Since both star formation and AGN activities require the accretion of matter, knowledge of the star formation history in the GC could give us a hint about its activity history.

There are already many works on the star formation history in the GC. Three young massive star clusters (the Arches, Quintuplet and Central clusters, 2-6 Myrs old, $\sim 10^4$ $M_\odot$, Figer et al. 1999, 2002; Genzel et al. 2003) were previously thought to be the major contributor of the star formation over the past 10 Myr. However, Dong et al. (2012) identify a similar number of evolved massive stars outside those three clusters, which indicate that significant star formation might also have taken place beyond the clusters. Nishiyama et al. (2016) find 13 intermediate-age stars that likely formed 50-500 Myr ago. Figer et al. (2004) study the stellar population in a number of GC fields and conclude that a continuous star formation history could best explain the data. Pfuhl et al. (2011) (see also Blum et al. 2003) investigate the star formation history in the central parsec of the GC and propose that the star formation rate (SFR) experienced a maximum at 10 Gyr ago, then decreased until 1-2 Gyr ago and increased again during the last several hundred million years. In a word, there is still considerable debate as to the precise star formation history of the GC.

A detailed study of stellar populations in the GC is seriously hampered by foreground extinction, which is not only large, with typical values A_{Ks} ∼2.5 (Schödel et al. 2010), but also changes on scales of arcseconds (Scoville et al. 2003; Schödel et al. 2007, 2010). The GC is totally obscured in the ultraviolet and optical bands, which would be optimal to distinguish between blue, young massive stars and red, old low-mass stars. In the near-infrared (IR), intrinsic colour indices are small ($J-K$ ≤1 mag and $H-K$ ≤0.3 mag), and the observed colours of stars at the GC are dominated by the extreme reddening. Without highly precise and accurate multi-band photometry, young massive stars can therefore be easily confused with less extinguished old, low-mass stars. Spectroscopy can identify late-type stars via their CO bandhead absorption. However, the need for high angular resolution limits observations to small regions (Maness et al. 2007; Do et al. 2009; Lu et al. 2013; Do et al. 2013, 2015; Støstad et al. 2015).

1.1. Variable Stars in the GC

Variable stars provide us with a tool to study the star formation history in the GC. Unlike apparent magnitudes, the periods and amplitudes of stars are unrelated to their foreground extinction. Stars with different initial masses evolve to certain stages and cross the instability strip in the Hertzprung-Russell diagram to become variables with different periods, amplitudes and luminosities (see more on this in §1.2). Therefore, such variables trace stellar populations of different ages, while their number densities could be used to infer the corresponding SFR at a given epoch. For example, Matsunaga et al. (2011) find three classical Cepheids in the central 40 pc of the GC, from which they derive a SFR of 0.075 $M_\odot$/yr about 20-30 Myr ago.

Monitoring stellar variability in the GC started in the 1980s (Haller & Rieke 1989). Early works can be roughly divided into two groups: 1) wide field-of-view (FoV) imaging with small telescopes (<4 meter) and 2) images and integral field units assisted by adaptive optics (AO) on 8-10 meter-class telescopes. The advantage of the former method is that the photometry is relatively stable for bright stars. The disadvantage is that the seeing-limited resolution is very poor, $\geq 1''$ and the confusion is severe for faint stars. The confusion limit problem can be largely alleviated by AO. However, AO has a small FoV (at least for the current almost exclusively used single-conjugated AO systems) and the point spread function (PSF) is potentially large at off-axis angles, larger than the so-called isoplanatic angle ($\sim 15''$ at 2 μm). In this latter case, the variability of the PSF can lead to systematic photometric errors of up to a few 0.1 mag (e.g., Schödel 2010). Additionally, the absolute zero point can be difficult to determine in AO observations of extremely crowded fields, when the PSF cannot be measured with high accuracy. Although this could be compensated by cross-calibrating different epochs with the help of presumably non-variable stars (e.g., Rafelski et al. 2007), zeropoint variations between epochs may remain an issue.

Instead, we will here use four-year baseline Hubble Space Telescope (*HST*) observations to identify variable stars in the Milky Way nuclear star cluster (MWNSC hereafter). These observations were obtained with the Wide Field Camera 3 (WFC3) IR camera. The large FoV ($123'' \times 136''$), high angular resolution (full width half maximum, FWHM, $\sim 0.15''$ at 1.5 μm), high sensitivity, stable PSF and accurate zeropoint (0.01 mag) of the observations allow us to accurately detect many dim variable stars with small amplitudes, except in the central few arcseconds around Sgr A*, where the source confusion remains too problematic. In this paper, we will use this dataset to produce a catalog of variable stars. In two follow-up papers (Dong et al. 2017b,c in preparation), we will use the RR Lyrae (hereafter RRL) stars to constrain the distance and old stellar population and to derive the binary fraction of massive stars in the MWNSC.

1.2. Types of Variable Stars

Periodic variable stars are classified according to their periods, luminosities, shapes of light curves and peak-to-peak amplitudes (PPAs). A complete summary of various types is beyond the scope of this paper. However, we briefly summarize the properties of some frequently encountered types: Long Period Variables (hereafter LPVs), Classical Cepheids (hereafter CCEPs), Type II Cepheids (hereafter T2Cs), RRLs and δ Scuti stars.

LPVs are red giant stars which vary on time scales from weeks to years and can be divided into three groups: regular variables (Miras), semi-regular variables (SRVs) and OGLE small amplitude red giants (OSARGs) (Soszyński et al. 2013). These stars evolve on the first-ascent red giant branch (RGB) or asymptotic giant branch (AGB). They occupy three out of five sequences ('A', 'B', 'C') identified in the period-magnitude diagram of Large Magellanic Cloud by Wood et al. (1999) and Wood (2000) (Soszynski et al. 2004). Among these three types, Miras are the best studied ones due to their large amplitudes: Their K band amplitudes are $\sim$0.6 mag on average (Wood 2000). Their period-luminosity (PL) relationship was first established by Glass & Lloyd Evans (1981) and Feast et al. (1989). They have been widely used as a distance indicator for remote galaxies. Frequently, SiO maser emission is observed from Miras, arising in the shells produced by outward propagating shocks (Gray et al. 2009). The colours of Miras are typically reddened by circumstellar dust produced in their slow, dense stellar winds. Compared to Miras, OSARGs and SRVs are dimmer by up to 1 mag at the K band (Ita et al. 2004).

CCEPs (1$\leq$P$\leq$100 d) are also well-studied and frequently used to measure the distance of remote galaxies, because of their brightness and regular variation. Their V band amplitude are $\sim$0.7 mag on average (Klagyivik & Szabados 2009). They are yellow supergiants with initial masses of 4-20 $M_{\odot}$ (Turner 1996). Their ages are $\sim$ 100 Myr (Becker et al. 1977) and their periods are anti-correlated with their ages and masses. Therefore, they can also be used as an age tracer for stellar populations (Alcock et al. 1999).

T2Cs are population II, old, low-mass and typically metal-poor stars often found in globular clusters, thick disk, bulge and halo of our Galaxy. Such variables are the immediate progeny of horizontal branch (HB) stars with little envelope mass (Catelan 2009). They have a similar period range as CCEPs, but are 1.5-2 mag dimmer (Sandage & Tammann 2006). Their amplitudes can reach up to 1 mag in the J and H bands. They can be divided into three groups according to their periods: BL Her stars ($1<P<4$ d), W Vir stars ($4<P<20$ d) and RV Tau (RV) stars ($20<P<100$ d) (Soszyński et al. 2008). These different types of variables represent the different evolutionary phases of low-mass stars after they leave the HB. Matsunaga et al. (2006) show that in the near-IR band, T2Cs follow a narrow PL relationship, which is not sensitive to the metallicity and can be used as a distance indicator.

RRLs ($0.2 \leq P \leq 1.0$ d, Catelan 2009) are old low-mass core-helium-burning giants (>10 Gyr, Walker 1989; Lee 1992) in the mass range of 0.55 to 0.80 $M_\odot$ (Marconi et al. 2015). According to the shape of the light curves, they can be divided into fundamental-mode (Type ab, hereafter RRab), first-overtone (type c, RRc hereafter) and rare double-mode (type d). RRab stars are on average intrinsically brighter and have higher amplitudes and longer period than RRc stars. Normally, the period of 0.4 d distinguishes RRab and RRc stars.

δ Scuti stars are main-sequence (MS) or early post-MS stars near the lower part of the instability trip (McNamara et al. 2007; Poleski et al. 2010). Their periods are less than 0.2 d. Compared to the four types above, they are fainter, have small PPA and are therefore very hard to be detected at the GC.

Besides the five types above, there exist other, but much rarer, variables, such as 1) red supergiant stars, evolved helium burning stars with initial mass between 10 and 30 $M_\odot$, with surface temperature 3000-4000 K (Verheyen et al. 2012); 2) luminous blue variables (LBVs), evolved massive stars with initial mass >30 $M_\odot$ (Crowther 2007); 3) OB main sequence stars (Lefèvre et al. 2009).

Finally, another frequently encountered class of variables consist of eclipsing/ellipsoidal binaries. For example, Soszyński & Udalski (2014) and Pawlak et al. (2014) suggest that binary scenario could explain the other two sequences ('D' and 'E') in the period-magnitude diagram of Wood et al. (1999) and Wood (2000), which are roughly 0.5 mag and 2 mag dimmer than Miras, respectively.

2. Observations and Data Reduction

2.1. HST Dataset

We focus on a field of $\sim 2.3' \times 2.3'$ ($\sim$ 5 pc $\times$ 5 pc) centered approximately on Sgr A*. This field was repeatedly observed by the WFC3 IR camera with the F153M filter from Jun, 2010 to April, 2014. The effective wavelength of the filter is 1.53 μm, which is close to the traditional Johnson/Glass H band ($\sim$1.63 μm). These observations came from two groups of *HST* programs: 1) Programs GO-11671, GO-12318, GO-12667 (PI, Andrea Ghez) and GO-13049 (PI, Tuan Do; Hosek et al. 2015; Støstad et al. 2015) observed Sgr A* with one pointing on each of Jun, 2010, Sep, 2011, Aug, 2012 and Feb, 2014, to study stellar proper motions and present-day mass function of the MWNSC; 2) Programs GO-13316 (PI, Howard Bushouse) and GO-13403 (PI, Nicolas Grosso) monitored Sgr A* from Feb, 2014 to April, 2014 (Mossoux et al. 2016), a period corresponding to the peri-center passage of the

G2 object around Sgr A* (Gillessen et al. 2012). These two programs included 56 pointings. The pointings and rotation angles of the observations from these six programs were different by less than 0.3″ and 3.1 degrees.

The time coverage of the data set can be divided into eight periods. Table 1 lists the observing dates, *HST* program IDs, durations, numbers of pointings and dithered exposures, as well as total effective exposure times. In summary, the 60 pointings consist of 290 dithered exposures; most of the pointings have four exposures, while the three pointings in 2010, 2011, 2012 have 21 exposures each and the one pointing in March 11, 2014 has three exposures. All these pointings have used a sub-pixel dithering pattern. The total exposure time is ∼90 ks. The exposure times for individual dithered exposures range between 250 s to 350 s. The durations of the eight observational blocks are from 0.3 hours to 15 hours. Because of the four-year time baseline of the total observations, as well as the duration of each period, this dataset can help us to identify variable stars with not only periods of years, but also periods of days.

We also used the *HST* WFC3/IR observations of the MWNSC in the F127M band (1.27 μm, an analog of the Johnson/Glass J band, 1.22 μm) from Programs GO-11671 and GO-12182 (PI, Tuan Do, Støstad et al. 2015, see also Table 1) to measure the F127M-F153M colours of variable candidates. This information was valuable to distinguish foreground/background stars from those belonging to the MWNSC. Program GO-11671 included one pointing consisting of 12 dithered exposures for a total exposure time of 7.2 ks. Its pointing and rotation angle were the same as the F153M observations in the same *HST* program. Program GO-12182 included nine pointings, each of which had four dithered exposures, totaling 1.8 ks exposure time. These pointings mapped the outer regions of the MWNSC, which were not covered by the Program GO-11671. They were used for variable candidates in the F153M band outside the FoV of Program GO-11671, but detected in the other programs, especially GO-13316 and 13403. Sub-pixel dithering patterns were employed. The observations in the F127M band were taken on Aug 17, 2010 and May 20, 2011, respectively.

2.2. Data Reduction

We first performed the basic reduction on the dithered exposures and combined them into mosaics. We downloaded *HST* raw data and calibration files from the Multimission Archive at STScI (MAST). We then used the *HST* pipeline, OPUS version and CALWFC3 version 2.1 to perform the basic calibration steps on individual dithered exposures, such as identifying bad pixels, bias correction, dark subtraction and flat fielding. In PyRAF, the 'Tweakreg' task aligned individual dithered exposures and the 'Astrodrizzle' task corrected

for the distortion, masked out defects (including cosmic rays), and combined the dithered exposures into a mosaic image. Considering the large proper motions of stars in the MWNSC[1], we used 'Tweakreg' and 'Astrodrizzle' tasks to produce one mosaic image per each year for the F153M observations. For demonstration purpose, we also constructed a mosaic image using all the 290 dithered F153M exposures, which is shown in the left panel of Fig. 1. Because the F127M observations were pointed toward different lines-of-sight, we produced mosaic images for each pointing, respectively. The method described in the appendix of Dong et al. (2011) was used to align the four F153M mosaic images and ten F127M mosaic images with an accuracy of 0.013", i.e., one tenth of the pixel size of the *HST* WFC3/IR camera.

The right panel of Fig. 1 shows a surface brightness image, produced by smoothing the image in the left panel, using a median filter with size of $2''$, more than ten times the FWHM of the WFC3/IR camera. This image is used to derive the photometric uncertainty discussed below. We divided the image into ten regions based on the logarithm of the surface brightness (in units of ergs s^{-1} cm^{-2} $Å^{-1}$ $arcsec^{-2}$) from -17.29 to -15.51 with a step size of 0.2 dex. The region with the lowest surface density has the smallest stellar density (see the left panel) and suffers extreme extinction because of the presence of a dark cloud. More information about these ten regions is given in Table 2.

The 'DOLPHOT' package[2] (Dolphin 2000) was then used to detect individual sources, extract photometry and perform artificial star tests. 'DOLPHOT' is a mature stellar photometry package, specifically developed for the analysis of the data taken by *HST* WFC3 and ACS and has been widely used in the *HST* treasury and large programs, such as the Panchromatic Andromeda Hubble Treasury (Dalcanton et al. 2012a) and the ACS Nearby Galaxy Survey (Dalcanton et al. 2012b). The 'DOLPHOT' package first aligns individual dithered exposures with their common stars. Then, the routine merges dithered exposures as a temporary merged image, on which the source detection is performed. For each dithered exposure, bright sources are used to determine the PSFs and aperture corrections at different locations in the WFC3/IR camera. Finally the routine measures stellar magnitudes not only in the temporary merged image, but also in the individual dithered exposures through the PSF fitting method with the centroid fixed to the spatial locations determined from the temporary merged image. 'DOLPHOT' also gives the photometric uncertainty,

[1] Schödel et al. (2009) study the proper motions of 6124 stars within 1.0 pc ($\sim 25''$) of Sgr A*. These stars could move on average 0.1 and even reach 1.28 WFC3/IR pixel (0.13″/pixel for the WFC3/IR camera) during the four-year time baseline of the F153M observations. These values decrease to 0.003 and 0.05 WFC3/IR pixels, if we consider only the observations from 2014.

[2] http://americano.dolphinsim.com/dolphot/

which only considers the Poisson fluctuations produced by the electrons in the camera. The 'DOLPHOT' parameters given in table 2 of Williams et al. (2014) were adopted, because they were well designed to detect faint stars in crowded regions. Due to the large proper motions, we performed the source detection for the F153M mosaics for each of the four years separately. On the other hand, at the F127M band, the source detection was performed on individual pointings.

The quality control parameters provided by 'DOLPHOT' were used to cull the output source catalog. These parameters are signal-to-noise ratio (S/N), sharpness, crowding, flag and 'CHI'. The 'sharpness' determines whether one object is a star or a cosmic-ray/extended background galaxy. The 'crowding' parameter expresses how significantly nearby bright sources affect photometry of dim sources. The 'flag' parameter indicates various problems, such as too many bad and saturated pixels or photometry aperture extending off the camera. 'CHI' is the reduced chi-square of the PSF fitting. The criteria given in Dalcanton et al. (2012a) were used: S/N > 4, sharpness$^2 < 0.1$ and crowd < 0.48, as well as flag ≤ 4, according to the 'DOLPHOT' menu. 'CHI' is normally not used to cull sources (Dalcanton et al. 2012a,b; Williams et al. 2014). However, this quality parameter seems to be related to some potential artifacts in the F153M light curves (see more discussion in §3 and Appendix B). We also removed the sources that were less than 5 pixels away from the CCD edge.

We merged the source catalogs. First, we used the astrometry information determined above to combine the four source catalogs in the F153M band. We searched among catalogs for the counterparts within $0.2''$ radius and ± 2 mag difference. The $0.2''$ searching radius is large enough to link high-velocity stars detected at different epochs. After that, we obtained the magnitudes of individual sources in the 290 dithered exposures. We kept only the sources detected in all four catalogs[3]. Finally, there were 33,070 sources left. Second, the F127M catalogs were corrected for the astrometry and cross-correlated with the F153M catalog. 29,526 F153M sources have available F127M magnitudes. Table 3 gives the ID, celestial coordinate in 2012[4], the mean F153M magnitude of the four catalogs and their corresponding uncertainty[5], as well as the F127M magnitude and uncertainty (σ_{F127M} hereafter), if avail-

[3]Because of the differences in the pointings and rotation angles, ∼10% of the FoV shown in the left panel of Fig. 1 has been observed by only the dithered exposures in 2014. We also kept the sources detected in this region.

[4]For the sources detected only in the FoV of the Programs GO-13316 and GO-13403, their celestial coordinates are those measured in 2014

[5]The F153M photometric uncertainty (σ_{F153M}, hereafter) is the largest value among the photometric errors from the four catalogs derived from the artificial star tests and the standard deviation of the four magnitude.

able. Table 4 gives the Julian dates, F153M magnitude (m_i, 'i' means the ith exposures), S/N, sharpness^2, crowd, flag and CHI of sources at individual dithered exposures.

The F153M magnitude distribution and the colour magnitude diagram (CMD, F127M-F153M VS F153M) are given in left panels of Fig. 2. The diagonal structure from [F127M-F153M, F153M]=[2, 17] to [3.6, 20] is caused by the Red Clump (RC) stars. The concentration of stars at [F127M-F153M, F153M]$\sim$[2, 21] is the RGB or MS stars in the foreground Galactic bulge. Three F127M$-$F153M colours, 1.7, 2.2 and 3.8 mag can be used to roughly divide our stars into the foreground, the less extinguished foreground Galactic bulge population, the GC population and the background (which corresponds A_K=1.6, 2.0, 3.5 by assuming the extinction law given in Schödel et al. (2010)). The sources with F127M$-$F153M>3.8 mag could also be red supergiants (such as IRS 7, $F127M$-$F153M$=4.0 mag) and AGB stars in the GC embedded in their circumstellar dust.

Artificial star tests were performed to determine the photometric uncertainty (σ_{F127M} and σ_{F153M}), magnitude variation among dithered exposures (σ_v, hereafter) and our detection limit. An artificial star catalog was produced for each source catalog, the luminosity, color and spatial distribution of which were similar to the observed sources. We used 'DOLPHOT' to repeatedly insert independent batches of artificial stars into the original dithered exposures at both the F127M and F153M bands. The number of artificial stars in each batch was not allowed to exceed 5% of the number observed, so that the surface density would not be significantly changed. The source detection of 'DOLPHOT' was run on these simulated images again. Thereafter, we divided the recovered artificial stars in each of the ten regions defined in the right panel of Fig. 1 by their magnitudes with a 0.5 mag stepsize. For each magnitude and surface brightness bin, we calculated 1) the median absolute value and 68% percentile of the difference between the output and input magnitudes in the mosaic images; 2) the standard deviation of the output magnitudes of the 290 dithered exposures. The values in 1) then characterize the absolute photometric uncertainties, $\sigma_{F127M}/\sigma_{F153M}$ and 2) determines the magnitude variation, σ_v, among the 290 dithered exposures. In 1), the former value represents the systematic error introduced by the confusion and the latter value is the statistic error. Finally, for each source, from their mean F153M magnitudes, or m_i, and local surface brightness, we interpolated the relationship determined above to obtain their σ_{F127M}, σ_{F153M} and $\sigma_{v,i}$. More discussion about the origin and meaning of σ_{F153M} and σ_v are given in Appendix A. Here, we just emphasize that since σ_{F153M} includes the systematic uncertainty introduced by source confusion, it overestimates the photometric variation among dithered exposures, especially for dim stars, while $\sigma_{v,i}$ does not show such a bias. Therefore, $\sigma_{v,i}$ will be used in §3 to identify variable stars.

Fig. 3 shows the comparison of $\sigma_{v,i}$ derived from the artificial star tests and the magni-

tude uncertainty given by the 'DOLPHOT' routine ($\sigma_{i,DOLPHOT}$). The former one is larger by up to 0.01 mag for stars with F153M < 21, but smaller for dimmer stars. In Appendix A, we found that the latter one could explain the magnitude variation among dithered exposures for the stars with F153M > 21 better. Therefore, for each star, we used the larger one of the two uncertainty measurements (artificial star test or formal uncertainty given by 'DOLPHOT') as the final $\sigma_{v,i}$, which is also given in Table 4. Fig. 4 presents the relationship between the F153M magnitude, m_i, and $\sigma_{v,i}$.

Fig. 5 shows the completeness as a function of the input F153M magnitudes for each of the four catalogs (the top panel) and regions with different surface brightness for the one in 2014 (the bottom panel). In the top panel, we find that even though the total exposure time in 2014 (227 dithered exposures, ∼68 ks) is more than nine times longer than those in 2010-2012 (21 dithered exposures and 7.3 ks for each year), the 90% (50%) completeness detection limits of the four years are similar: ∼17.4 mag (19 mag). This illustrates that the observations are limited by confusion, and increasing the exposure time does not lead to the detection of more faint stars. The 90% (50%) completeness detection limits of different regions are given in Table 2. In the F153M band, we can detect sources in the lowest surface brightness region that are 6 mag fainter than in the highest surface brightness region.

3. Methods

We used the least χ^2 method to select variable stars. For each source,

$$weight_i = \frac{1/\sigma_{v,i}^2}{\sum 1/\sigma_{v,i}^2} \tag{1}$$

$$\bar{m} = \sum m_i \times weight_i \tag{2}$$

$$\chi^2/d.o.f = \sum_i \frac{(m_i - \bar{m})^2}{\sigma_{v,i}^2}/(n-1) \tag{3}$$

where 'n' is the total number of dithered exposures used and the sums are over the 'n' exposures. We only accepted the photometry from the dithered exposures with S/N_i >4, $sharpness_i^2$ <0.1, $crowd_i$ <0.48 and $flag_i$ <=4. At least three data points ($n \geq 3$) are needed to calculate $\chi^2/d.o.f$.

We analyzed the variability in two categories: among years (long-term) or days (short-term). For the former case, all 290 dithered exposures are used to calculate χ^2/d.o.f (χ_y^2 hereafter, the subscript 'y' means 'year'). For the latter case, we used only the dithered exposures in three periods: groups 5, 6 and 7 in Table 1. These groups are characterized by

long-duration observations (≥10 hours). We derived χ^2/d.o.f for each of the three periods and used the maximum value (χ^2_d hereafter, the subscript 'd' means 'day') as the criterion for whether a star is variable or not. We added 0.025 and 0.01 mag systematic uncertainties to $\sigma_{v,i}$, when calculating χ^2_y and χ^2_d, respectively (see Appendix A). Table 3 gives the χ^2_y and χ^2_d for individual sources. Table 5 gives the 68% and 90% dispersions, as well as the median of the χ^2_y and χ^2_d values. The median values are around one, which means that $\sigma_{v,i}$ is reasonably estimated. Fig. 6 gives the cumulative distribution functions of χ^2_y (the green lines) and χ^2_d (the black lines). As expected, χ^2_y extends to larger values than χ^2_d because the latter is not sensitive to long-term variables.

When visually examining light curves of individual sources, we found that the majority of sources with large χ^2_d showed rapid, alternating intensity variations among dithered exposures (e.g., Fig. 7). These sources widely distribute in the detector, but preferred the regions with high surface brightness. Although we could not exclude the possibility that this variability was real for some individual stars, we suspected that this phenomenon was typically due to instrumental effects (see more discussion in Appendix B). Therefore, we binned the data for individual sources to reduce this effect on the derived χ^2_d and χ^2_y. For the 57 pointings in 2014, we binned the dithered exposures in individual pointings. For each of the three pointings from 2010 to 2012, we divided the 21 dithered exposures into five bins (the first four bins include four dithered exposures, while the last one includes five exposures), so that each bin has similar total exposure time to those in 2014. Therefore, in Eqns.(1)-(3), m_i is the mean magnitudes of these dithered exposures in each bin and the uncertainty is the maximum of their standard deviation and their $\sigma_{v,i}$, then divided by the number of dithered exposures in each bin. Using the standard deviation of magnitudes of individual dithered exposures can cause the pointings with outliers in magnitude to have larger uncertainty and lower weight in the final reduced $\chi^2/d.o.f$, while using the $\sigma_{v,i}$ can prevent the bins which have very similar magnitudes among dithered exposures in these bins to have overly small uncertainty and too much weight in the reduced $\chi^2/d.o.f$. The next step was to use Eqns. (1)-(3) to derive $\chi^2_{y,b}$ and $\chi^2_{d,b}$ (the extra subscript 'b' means 'bin'), which are also given in Table 3. Table 5 gives the statistic distributions of $\chi^2_{y,b}$ and $\chi^2_{d,b}$ and Fig. 6 gives their cumulative distribution functions (green and black dotted lines). From the cumulative distribution, we conclude that the difference between χ^2_y and $\chi^2_{y,b}$ is smaller than that between χ^2_d and $\chi^2_{d,b}$.

By using the procedure given in §3, we found 3879 and 77 sources in our two categories with variability over the four-year baseline and within one day, respectively. The former sources have χ^2_y>3, $\chi^2_{y,b}$>3, while the latter have $\chi^2_d > 2$, $\chi^2_{d,b}$>2. 42 stars fall in both categories.

Further visual examination was carried out individually for all these variables by six

people (HD, RS, FN, EG, TG and Siro Benvenutto Gallego, the son of EG). We only considered a source as a real variable star, if it was selected by more than half of us. This examination was useful to remove sources with apparently large χ^2, caused by potential artifacts. In total, 34 and 4 stars are removed from the two categories as non-variable stars. On the other hand, we also included 3 additional sources: IDs 2495, 11656 and 12097, with $\chi^2_d > 2$, $\chi^2_{d,b} < 2$ due to large photometric uncertainty, as potential candidates having periods of days. In the final tally, there are 3894 variable candidates: 3845 and 76 sources are in the two categories, respectively, and 27 candidates are in both. These sources are listed in Table 3.

4. Results

The right panel of Fig. 2 and Figs. 8 and 9 show the magnitude distribution, CMD, the fraction and PPA distributions of variable stars. The variable candidates are widely distributed throughout the CMD. indicating their strong differential reddening and various origins. Except for a few foreground stars, the majority of variable candidates should be in the Galactic bulge or MWNSC, according to their F127M-F153M colour. Fig. 8 indicates that the fraction of variable stars is roughly 15% for all the magnitude ranges and increases with the F127M-F153M color. Especially, 51% of stars with F127M-F153M>3.8 are variables. The PPA distribution of variable stars has a peak around 0.5 mag.

Fig. 10 shows examples of light curves for non-variable stars, while Fig. 11 illustrates light curves for stars which vary among years. This sample of stars covers a large F153M magnitude range from $\sim$ 12 to 20 mag. The first three sources in Fig. 10 exhibit very little variation, if any; The standard deviations of their magnitudes are smaller than 0.014 mag. While the deviation increases to 0.04 mag for ID 23389, the large $\sigma_{v,i}$ $\sim$0.1 mag excludes it as a variable star. In contrast, the six stars in Fig. 11 all show large variations with PPAs from 1 (ID 448) to 2 mag (ID 6784). The magnitudes of IDs 43, 2201, 6784 and 13873 with $\chi^2_d > 2$ also vary on daily timescale.

From the light curves, we divided our 76 stars with intraday variability into three subgroups, based on the difference in their observed light curve characteristics:

- Subgroup 1: Stars with a significant fraction of their periods covered by our dataset, especially by the observation block on April 2-3, 2014. The periods of these stars can be accurately determined (see more discussion in §5.3.2). Figs. 12 to 14 show the light curves for the 28 stars in this subgroup.

- Subgroup 2: Eclipsing binary candidates, with the dips being a small fraction of their

periods, fortunately covered by our dataset (Fig. 15). ID 1365, a known contact massive eclipsing binary system (E60 in Pfuhl et al. 2014), shows a sinusoidal light curve. The other stars in this subgroup show similar features in their light curves: the magnitudes are roughly constant for awhile, become dimmer during a short period and quickly return to their constant value. Except for IDs 2980 and 21717, the periods of the other sources seem to be longer than those in subgroup 1 (see more discussion in §5.3.1).

- Subgroup 3: The remaining sources cannot be unambiguously assigned to any variability subgroup, because our dataset only includes a small fraction of their periods, due to the poor temporal sampling. Fig. 16 gives nine examples.

As a next step, we tried to derive the periods of some short-term variables. Because large gaps, from 10 to 547 days, exist between the observing runs in Table 1 and the longest duration of any individual observing run is only 15 hours, it is not possible to unambiguously determine the periods for most of our variable candidates. We focused on stars in Subgroups 1 and 2. We used the Lomb-Scargle periodogram (Lomb 1976; Scargle 1982) technique to calculate the periods of 36 stars given in Figs. 12 to 15 (except for ID 30400 in Fig. 15, because its light curve includes only one dip). Specifically, we used the IDL routine 'lomb.pro' to perform the calculation. The routine calculates the power spectral density of the Fourier components of the light curves. The routine does not account for the binary nature of eclipsing systems, so treats the two dips in the light curves of eclipsing binary candidates as the same origin. Therefore, we doubled the period derived from the periodogram analysis for these sources. The IDs, periods, F153M magnitudes and colours of the 36 sources are given in Table 6.

5. Discussion

In this section, we first compare our results with previous works in §5.1 to check the efficiency of our method and dataset to identify variables. Then, in §5.2 we cross-correlate our source catalog with existing catalogs having spectroscopic identifications. We discuss the variable types for the stars with determined period in §4 and then statistically classify the other variables without period measurements in §5.3 and §5.4, respectively.

5.1. Comparison with Previous Work

The reliability of our variability analysis can be assessed by comparing our results with those of prior studies. Table 7 summarizes existing variability studies in the GC, the instruments that were used, the FoV and covered time range, as well as the total number of variables found and the number that we recovered.

Variability studies of the GC began in the 1980s (Haller & Rieke 1989). Small telescopes (< 4 m) were used to observe the GC in a relatively small number of epochs. Therefore, these studies could only identify variable stars, but could not give their periods. Tamura et al. (1996) and Blum et al. (1996) reported IRS 7, 9, 12N, 28, 14SW and 10E (IRS 10E* or IRS 10EE) to be variable stars, all of which were also identified as variables by our method.

Some long-term monitoring studies of the GC with large FoV camera were published later (Glass et al. 2001; Matsunaga et al. 2009, 2011, 2013; Peeples et al. 2007). Glass et al. (2001) reported 409 LPV candidates in the central $24' \times 24'$ field, 10 of which fall into our FoV. Three of these 10 stars failed to appear as variables in our study for good reasons: two with periods of $\sim$ 350 d are near the edge of our FoV, detected only in March and April 2014, while the other, '3-2389' in Table 2 of Glass et al. (2001), has a very long period of 408 d and a K band amplitude of 1.4 mag. '3-2389' has been detected in a SiO maser survey (Deguchi et al. 2004) and should be a Mira. In our dataset, its magnitude increased 0.1 mag from 2010 to 2012, and then appeared constant from February to April, 2014. Therefore, our dataset could miss the part of light curve in which the magnitude changes significantly.

Matsunaga et al. (2009, 2011, 2013) identified 549 Miras, three CCEPs, 18 T2Cs, 24 eclipsing binaries, one pulsating star and one Cepheid-like variable from the SIRIUS survey[6], which monitored the central $20' \times 30'$ field from 2001 to 2008. Only 17 of their Miras fall into the FoV of our dataset, two of which are not classified as variables by us. One is near the edge of our FoV, only detected in April, 2014. The other one is '604' in Table 6 of Matsunaga et al. (2009) with H=12.48 and PPA in the H band = 0.38 mag. According to its celestial coordinate, its counterpart should be ID 105 ($0.06''$ away) in our catalog, with F153M = 13.5 mag, χ^2_y=1.6 and PPA = 0.17 mag, a non-variable source in our catalog. Instead, about $4.4''$ away, ID 87 is variable and has F153M=13.4 mag , χ^2_y=9.4 and PPA=0.32 mag. We suspect that maybe ID 86 is the real counterpart of '604' in Matsunaga et al. (2009).

[6]Simultaneous 3-colour InfraRed Imager for Unbiased Surveys (SIRIUS) was taken by the Infrared Survey Facility (IRSF) in South Africa, with a pixel scale of $0.45''$ (Nagayama et al. 2003). The survey includes the region $|l| < 2$ degree and $|b| < 1$ degree.

Peeples et al. (2007) reported 98 variable stars and 14 stars with well defined periods separately in their Tables 1 and 2. 94 and 14 of them fall into our field-of-view and 37 and 11 are classified by us as variables. Because Peeples et al. used a crude root-mean-squared cut method to identify variable stars (log (rms) > a×m_o +b, where 'rms' and 'm_o' are the standard deviation and mean of the observed magnitudes, while 'a' and 'b' are coefficients defined by Peeples et al.), we suspect that their catalog contains many false variables. Therefore, we concentrate on their stars with well defined periods. Among the three of the 14 stars, which are not classified as variable in our dataset, PSDJ174540.25-290027.2 (IRS 16NE) has been considered to be photometric non-variable in many references, such as Rafelski et al. (2007) and Pfuhl et al. (2014). Its light curve in Fig. 12 of Peeples et al. (2007) is very noisy. We suspect that the period claimed by Peeples et al. (2007) is due to some instrumental effects. The other two stars are PSDJ174535.60-290035.4 and PSDJ174540.16-290055.7. We checked sources near them in Table 3, and found that, while the magnitudes of some of them seem to change from 2010 to 2012, they do not pass our selection criteria. Therefore, these two sources need further investigation.

Ott et al. (1999) performed the first high-angular-resolution variability study of the GC (FWHM ∼0.15″), using the speckle camera SHARP on the ESO NTT. They also used the least χ^2 method and found that 122 of the 218 stars in their sample with m_K <13 showed variability larger than 3 sigma. In particular, they first reported that IRS 16SW (ID 43, in Fig. 11) is an eclipsing binary. In our data set, 195 of their 218 stars have counterparts, 115 of which are variables, according to Ott et al. However, only 32 of the 195 stars are identified as variables by our method. Fig. 17 compares the reduced χ^2 of the 195 stars from Ott et al. and our dataset. There is no clear correlation. We suggest that this inconsistency could be due to two problems in the method used in Ott et al.: 1) Unsuitable choice of flux calibrators. Ott et al. anchored the photometry to eight stars, including IRS 16C, IRS 16NW and IRS 29N, which they assumed to be non-variable, even though they found that the reduced chi-squared of IRS16C reaches 4.1. Instead, Rafelski et al. (2007) identified IRS 16NW and IRS 29N (see also Hornstein et al. 2002) as variable stars with ∼0.2 mag variation in the K band. Our dataset identified IRS 29N as a variable star as well, with PPA equal to 0.66 mag in the F153M band. IRS 16C has χ^2_y=4.7, $\chi^2_{y,b}$=2.0 and PPA=0.3 mag. The systematic uncertainty introduced by the unsuitable flux calibrators could have led to the misidentification of some bright non-variable sources with small photometric uncertainties as variable stars. Instead, for our *HST* dataset, the systematic uncertainty of its photometric zeropoints is only 1%. 2) Ott et al. determined the photometry using three methods with the same empirical PSF extracted from the images. The standard deviation of the photometry derived from these methods is used to represent the real fluctuation variation among exposures. We suspect that this method could underestimate the real uncertainty, especially for the dim stars. For

example, Fig. 18 shows the K band magnitude distribution (m_K, from Table 2 in Ott et al.) for the variable stars defined by Ott et al., but classified as non-variable (solid line) and variable (dashed line) stars by our dataset. 30% in the former case have m_K >12.5, while this value decreases to 12.5% for the latter cases.

Since 2005, more long term observations of the GC taken by 8m-class telescopes have become available. Rafelski et al. (2007) performed a variability study in the central 5″ with a 10 year baseline observation with Keck/NIRC camera. They found 15 variables out of 131 stars with m_k<16. Compared to their study, which reaches an angular resolution of about 0.06″, in this region, our dataset suffers from confusion due to the poor resolution. Therefore, only 10 of their 15 variables are detected and only 3 of those ten stars, IRS 16SW, IRS 29N and S0-34 have been identified as variables. Both IRS 16NW and IRS 16CC[7] are classified as variable by Rafelski et al., but not by us (PPA=0.22 mag and 0.16 mag), or by Ott et al. (1999) or Pfuhl et al. (2014). Pfuhl et al. (2014) used *VLT*/SINFONI spectroscopy and NACO imaging data from 2003 to 2013 and identified IRS 16NE as a non-variable star in photometry[8] and E60 as a close WR eclipsing binary with a period of 2.276 days, which are consistent with our dataset (IRS 16NE: ID 14, E60: ID 1365). Thanks to the stable performance of the *HST*/WFC3 IR camera, our light curve for E60 (the top left figure in Fig. 15) has significantly smaller photometric uncertainties than that taken by the NACO camera on the 8 m *VLT* telescope (Figure 3 in Pfuhl et al. 2014).

Besides near-IR variability, Reid et al. (2007) found 15 SiO masers within 50″ of Sgr A*, 11 of which are not associated with any LPV candidates given in Glass et al. (2001). We find near-IR counterparts for all of these maser stars, except for IRS 19NW, SiO12 and SiO 17. The *HST* WFC3/IR image did not allow us to disentangle IRS 19NW from the bright non-variable IRS 19 (ID 26, F153M=12.2 mag, χ^2_y=0.55, $\chi^2_{y,b}$=0.26), while the giant counterparts of SiO 12 and SiO 17 could be background stars that are not detected because of large foreground extinction. 11 of the 12 masers that we detect are classified as variable stars; SiO11 does not fully pass our criteria (χ^2_y=5.3, $\chi^2_{y,b}$=2.9, PPA=0.28), but its variability is apparent in its light curve.

Table 8 summarizes the cross-correlation between our source catalogs and those in the previous variable studies. In summary, the four-year baseline *HST*/WFC3 observations used here form a unique dataset for identifying variable stars in the GC, except in the central few arc seconds, due to the strong source confusion there. Thanks to the stable photometric

[7] Rafelski et al. (2007) classify IRS 16CC as variable at the 'L' band, not the 'K' band.

[8]The radial velocity of IRS 16NE change with a period of 224 days, which suggests that it is a binary system. The non-variability in its photometry could probably be due to the inclination angle.

zeropoint of these observations and the method which we used to determine $\sigma_{v,i}$, we are able to confirm most of the well-measured variable stars found in previous work.

5.2. Cross-correlation with Spectroscopic Catalogs

In this subsection, we cross-correlate our variable source catalog with existing spectroscopic observations, which will help us understand their stellar types. Specifically, we compare with 1) Paumard et al. (2006), Bartko et al. (2009) and Feldmeier-Krause et al. (2015), which concentrate on massive stars; 2) Maness et al. (2007) and Feldmeier-Krause et al. (2017), which focus on late-type stars; 3) Blum et al. (2003), Do et al. (2013), Støstad et al. (2015) and Nishiyama et al. (2016), which include both early-type and late-type stars. Most of the targets of the spectroscopic observations are brighter than 16 mag in the K band.

Table 9 summarizes our variable star candidates with spectroscopically studied counterparts. In total, Paumard et al. (2006), Bartko et al. (2009) and Feldmeier-Krause et al. (2015) identify (or tentatively classify) 153 WR stars, OB supergiants and main-sequence stars. We detected all of them, except for 22 near Sgr A* due to confusion. 38 of these 131 stars are identified as variables. The cause of variability of these early-type stars is probably binarity or confusion with other sources. We will give a more thorough discussion of the binary fraction of massive stars in the MWNSC in Dong et al. 2017c (in preparation). Maness et al. (2007) and Feldmeier-Krause et al. (2017) list 329 and 990 late-type stars (i.e. cool stars with molecular CO absorption lines[9]), 21 and 223 of which, respectively are variables, according to our detections. Blum et al. (2003) derive surface temperatures and bolometric luminosities for 79 stars in the GC, which includes AGB and supergiant stars. 78 of these 79 stars fall into our FoV and are divided into three groups (according to Blum et al. 2003): 20 as Miras, 43 as giants (III), 15 as supergiants (I). We identify 17 (85%), 17 (40%) and 4 (27%) of the stars in these three groups respectively as variables. Do et al. (2013), Støstad et al. (2015) and Nishiyama et al. (2016) report 286, 371 and 20 stars, respectively, including 86 early-type stars (i.e. hot stars without CO absorption lines, definitely related to recent star formation), 536 late-type stars and 55 without spectral identifications. 29, 16 and 7 of the stars listed by Do et al. (2013), Støstad et al. (2015) and Nishiyama et al. (2016) show variability. Except for 7 and 5 variable stars in Do et al. (2013) and Nishiyama et al. (2016), all the other variable stars are defined as late-type stars.

[9]Late-type stars (F-type or later, Do et al. 2015) are not equivalent to evolved, low mass stars, such as AGB stars or RGB stars. Late-type stars could also be red supergiants (luminosity class I), related to recent star formation, for example, IRS 7 (Carr et al. 2000; Pfuhl et al. 2011; Feldmeier-Krause et al. 2017).

In summary, 319 variable stars in our catalog have available spectroscopic identifications, which includes 13 WR stars, 19 OB stars, 4 supergiants, 13 early-type stars, 18 Miras, 17 giants and 235 late-type stars.

5.3. Classifying Variables with Well-Determined Periods

In this subsection, we attempt to assign variability types to our identified variables having well-determined light curves and measured periods. Those without period measurements are considered in the next subsection.

5.3.1. Eclipsing Binaries

Depending on the distances between stars and their sizes, eclipsing binaries can be divided into detached, semidetached and contact binaries. Since the stars in a detached binary are still within their Roche lobe and evolve separately, the light curve stays constant except when one star eclipses the other. The depth of the dip caused by the eclipsing depends on the relative sizes of the two stars. In a contact binary, the two stars are so close to each other that their filled Roche lobes interact. As a result, there is no plateau in the light curves. The light curve of a semidetached binary lies between those of the detached and contact binaries.

There are ten eclipsing binaries in our variable catalog (ID 43 in Fig. 11 and nine in Fig. 15). Most of them should be detached binaries, for example, most of those in Fig. 15. Among them, ID 2980 shows quick variation with a period of $\sim$0.5 d. The difference in the depth of the dips excludes the possibility that the variation is due to a pulsating single star (see top right panel in Fig. 15, especially in Group 5 with modified Julian dates $\sim$ 3.2 d). The other three, ID 43 (IRS 16SW, Rafelski et al. 2007), ID 1365 (E60, Pfuhl et al. 2014) and ID 217171 are contact binaries, the light curves of which have a sinusoidal shape. According to the F127M-F153M colours of the ten eclipsing binaries given in Table 6, two of them, ID 1404 and ID 2980, are in the foreground, three are in the Galactic bulge and the other six, including ID 43 and ID 1365, are within the GC.

Our variable star catalog may contain unclassified eclipsing binaries. The periods as well as the duration and amplitude of eclipses are determined by physical parameters of the binary systems. Due to inadequate sampling, however, our data may not cover the light curves of many potential binaries adequately. Therefore, a significant fraction of the 76 stars with intraday variability could be eclipsing binaries.

In addition, sources that have not been detected as variables may also be eclipsing binaries. The depth of the dip caused by an eclipse in the light curve of a binary is a strong function of the relative sizes of the stars and their orbital inclination angle. Such a dip, especially in a long-period binary, may be missed in an observation. Future observations taken by the *HST*/WFC3 with optimal cadences are highly desirable to confirm our binary candidates and find new ones. Of particular interest are massive binaries (see Dong et al. 2017c, in preparation), which may provide useful insights into star formation processes in the unique environment of the MWNSC.

5.3.2. δ Scuti, RRL and T2C

Among the 28 stars shown in Figs 12 to 14, 4, 8, 13 and 3 of them have periods of <0.2, 0.2-0.4, 0.4-1 and >1 d, the expected ranges for δ Scuti, RRc, RRab and Cepheids, respectively. Here we discuss these classes of variable candidates individually:

δ **Scuti**: The four δ Scuti candidates are IDs 6164, 12215, 20785 and 29285, with PPA=0.33, 0.25, 0.40 and 0.75 mag. The OGLE survey (Poleski et al. 2010) shows that the I band amplitude of a sample of the δ Scuti stars is 0.21±0.1 mag, although the maximum amplitude at the I band could reach 0.9 mag. Therefore ID 20785 may have a too large amplitude in the F153M band to be δ Scuti and may instead be an eclipsing binary system. According to the F127M-F153M colours, ID 29285 is likely in the foreground, while the other three sources are in the Galactic bulge.

RRLs: a detailed analysis of the 21 stars with periods between 0.2 and 1 d will be presented in Dong et al. 2017b (in preparation). They report discoveries of 3 RRcs and 4 RRabs, plus three RRab candidates. In particular, IDs 8735, 10520, 22197 and 22312 show the typical sawtooth light curves of RRabs.

T2C: The three sources with periods > 1 d could be CCEPs, T2Cs or eclipsing binaries. The key differences between the first two types are their intrinsic luminosities, while the last one does not follow the PL relationship of CCEPs or T2Cs. We adopted Equations (6)-(11) in Matsunaga et al. (2013) as the PL relationships for CCEPs and T2Cs. Their J and H are for the SIRIUS filters (J: 1.25 μm and H: 1.63 μm). Because of the different effective wavelengths, the absolute magnitudes at F127M/F153M bands are not the same to those at the J/H bands, especially for cool stars with strong water vapor absorption at the J and H bands (Lançon & Wood 2000). For example, the Mira-type LPV S Car, the near-IR spectrum of which is given in Figure 8 of Lançon & Wood (2000) has F153M - H=0.23. Therefore, we used the method given in the Appendix of Dong et al. 2017b to calculate

the transformation from the SIRIUS to WFC3/IR absolute magnitudes through the stellar atmosphere model of Castelli & Kurucz (2004) with surface temperatures between 3500 K and 10^4 K:

$$F127M = J_{SIRIUS} - 0.006 - 0.109 \times (J_{SIRIUS} - H_{SIRIUS}) \quad (4)$$

$$F153M = H_{SIRIUS} - 0.004 + 0.184 \times (J_{SIRIUS} - H_{SIRIUS}) \quad (5)$$

With the extinction law of Schödel et al. (2010)[10], the same method is used to derive the relative extinction, A_{F127M}=1.49A_{F153M} and A_{F153M}=2.08A_{Ks} (*VLT*/NACO K_s, 2.18 μm). Then from the F127M and F153M apparent magnitudes we derived their extinctions and distances, as listed in Table 10. We can see that if the three sources were CCEPs, they would be too far away to be in the Milky Way. ID 23605 is more likely a short-period T2C, i.e. BL Her star, probably only slightly beyond the GC. If ID 23523 and ID 26112 were T2C stars on the far-side of the Galactic disk or halo, then they would suffer less extinction than the average of the MWNSC, which is extremely unlikely. They might therefore be mis-classified eclipsing binaries. Fig. 19 gives the CMDs of detected sources within 2″ of the three T2C candidates. ID 23605 is redder than the majority of nearby sources, while ID 23523 and ID 26112 are not. This supports our typing of these three sources, i.e. ID 23605 is a T2C star, while IDs 23523 and 26112 are eclipsing binaries.

5.4. Classifying variables with no measured period

Only a tiny portion of our 3894 variable stars have spectroscopic observations (8.2%) or determined periods (1%), which are important for the classification. We therefore only statistically study our unclassified variable stars, based on their locations in the CMD, compared with those variable stars having existing spectroscopic identification in the CMD (F127M-F153M vs F153M, Fig. 20), and compare with the magnitudes and colours of four well-known types of variable stars (Fig. 21).

Fig. 20 shows all our variable candidates in the CMD. Stars classified through spectroscopy are overplotted in red open symbols, while stars classified via their light curves and

[10]The extinction law given in Nishiyama et al. (2009) with a slope of -2.0 is flatter than that given in Schödel et al. (2010). Schödel et al. (2010) obtain the law from RC stars detected by *VLT*/NACO, while Nishiyama et al. (2009) constrain the slope from the observations taken by the 1.4 m IRSF telescope on the central 3×1 degree, which suffer from strong confusion in the central few arc minutes. Therefore, we prefer the extinction law given in Schödel et al. (2010) because it was obtained with high angular resolution observations very close to the field that we are studying.

periods are shown as yellow filled symbols. Most of the stars with spectroscopic identifications are brighter than 18 mag at the F153M band, because of the sensitivity limits of such observations. On the other hand, the stars with variable types determined from only their periods concentrate in fainter parts of the CMD. That is partly due to the origins of these variable stars: 1) δ Scuti and RRL stars are known to be dim; 2) T2Cs with periods of $\sim$1 d are dimmer than those of 10 and 100 days by $\sim$ 2.4 and 4.8 mag at the F153M band, according to their PL relationship.

The PL relationships of Miras, CCEP, T2C and RRL provide us with intrinsic luminosities and colours. Applying the distance modulus of the GC (8.0 kpc) and using foreground extinction (A_K=2, 2.5, 3, 3.5 mag), we overlay the potential locations of these stars on the CMDs shown in Fig. 21. The PL relationships for CCEPs and T2Cs are given in §5.3.2. For Miras, we used Equations (1) and (2) of Matsunaga et al. (2009) derived from Miras in the LMC. Whitelock et al. (2008) suggest that the relationships in the LMC and Galactic bulge are similar. The PL relationships for RRL are given in Equations (4) and (5) of Catelan et al. (2004) from theoretical calculation, assuming the metallicity, $[Fe/H]$=-1.0 (Walker & Terndrup 1991). The J and H in Matsunaga et al. (2009) and Catelan et al. (2004) are for the SIRIUS filters and Johnson-Cousins-Glass system (J: 1.22 μm and H: 1.63 μm), respectively. As in §5.3.2, we used the same method given in the Appendix of Dong et al. 2017b to calculate the transformation from the Johnson-Cousins-Glass (JCG) system to WFC3/IR magnitudes:

$$F127M = J_{JCG} - 0.007 - 0.142 \times (J_{JCG} - H_{JCG}) \quad (6)$$

$$F153M = H_{JCG} - 0.005 + 0.198 \times (J_{JCG} - H_{JCG}) \quad (7)$$

The relative extinction A_{F127M}/A_{F153M} given in §5.3.2 is also used. We can see that the brightness decreases from Miras, CCEP, T2Cs to RRL. Miras are the reddest sources among them.

In the following, we discuss the potential contributions to our variability sample of these different types of stars.

WR, OB MS and Red supergiant: Red supergiants, like IRS 7, are known for their variations with periods of years and amplitudes of about 1 mag (Kiss et al. 2006). On the other hand, variability of single WR and OB stars tends to have small amplitude ($\sim$0.1 mag in the visual band, Figure 9d in Lefèvre et al. 2009). Therefore, variable WR and OB stars in our dataset are likely to be eclipsing binary systems (PPA=0.67$\pm$0.44 mag, mean and standard deviation; more discussion will be given in Dong et al. 2017c, in preparation). However, such massive stars could only explain a small fraction of the variables without spectroscopic identifications for several reasons: 1) Red supergiants are very bright; for

example, IRS 7 has $K\sim$ 7 mag (Carr et al. 2000). With 1 mag amplitude, the variability of such stars should easily have been detected in previous long-period monitoring programs conducted with $<$ 4m telescopes (see §5.1); 2) The sample of WR stars in the MWNSC, should have been roughly complete, except for dusty WC stars with red and featureless spectra (Dong et al. 2012); 3) Recent works (Støstad et al. 2015; Feldmeier-Krause et al. 2015) have found 90% of the young massive stars within 0.5 pc (i.e. 12.5″) of the GC. But this region only includes ∼3.5% of the variables in our catalog.

CCEP: The magnitude and colour ranges of CCEP well match with the range of variable stars having F153M $<$ 18 mag and F127M - F153M $<$ 4. Matsunaga et al. (2011, 2015) found four CCEPs in the GC. According to the SFR given in Matsunaga et al. (2011) and Pfuhl et al. (2011), we estimate that less than 1 CCEP should be in our FoV.

However, in §5.2, we found that 5 of the 13 stars of age 50-500 Myr and in the K magnitude range from 10.2 to 11.5 mag, as given in Nishiyama et al. (2016), are in our variable catalog. Their light curves are given in Fig. 22 and we have marked their location in the top right panel in Fig. 21. Except for ID 423, which has been only detected in the observations before Feb 28, 2014, the other four sources show clear variability among the exposures from Feb to Apr, 2014. Their location in the CMD (Fig. 21) could also been explained by the PL relationship of CCEP with A_K=2 to 3 mag. If we assume that these stars are in the MWNSC, we can use the extinction map of Nogueras-Lara et al. (2017, in preparation)[11] to derive their absolute K band magnitude. Then by using the Equation 11 of Matsunaga et al. (2013), we can derive their periods, between 14.5 d to 24.0 d, which are similar to those of the four CCEPs identified by Matsunaga et al. The reasons why SIRIUS survey did not identify these CCEP candidates are probably 1) they are relatively dimmer at the K band due to the higher extinction and 2) SIRIUS observations suffer from strong confusion in the central few arc minutes. The only concern is their surface temperatures, between 3850 K to 4670 K, which are near the lower limit of the instability strip of Cepheids (Fiorentino et al. 2002). However, considering the large temperature uncertainty given in (Nishiyama et al. 2016), ∼150 K, we cannot use their temperatures to conclude that they are not CCEPs.

Single Red Giant Stars: Miras tend to be brighter than 16 mag and are located in the top right part of the CMD. However, sometimes such stars can have strong dusty winds and thus account for most variable stars with F127M-F153M$>$3.8, 51% of which are variables (see Fig. 8). Although OSARGs and SRVs are roughly one mag dimmer than Miras at the K band, but still brighter than Cepheids ('G' and 'F' sequences for CCEPs and T2Cs

[11]Nogueras et al. (2017, in preparation) produce an extinction map of the GC with a spatial resolution of ∼2″ from the RC stars detected in VLT/HAWK-I survey of the central 100 pc at J, H and K bands.

in Figure 6 of Ita et al. 2004). Therefore, they cannot explain the majority of our variables with F153M > 18 mag.

T2C: As shown in Fig. 20, the colour and magnitude ranges of T2Cs are consistent with the majority of our variables. Soszyński et al. (2011) also suggest that the Galactic bulge contains a significant population of T2Cs with a centrally concentrated distribution.

The problem with T2C stars is that they are metal poor ([M/H]<0) and are widely found in the low metallicity region, such as globular clusters, thick disk, bulge and halo of the Galaxy (Wallerstein 2002). Feldmeier-Krause et al. (2017) claim that only 6% (22%) of sample stars (<700) towards the GC have [M/H]<-0.5 (0) (see also Do et al. 2015). On the other hand, Matsunaga et al. (2013) identify 16 T2C in the GC, all within the range of 12.9<H<15.3. These stars may represent the bright end of the luminosity function of T2Cs towards the GC. From the PL relationship, Matsunaga et al. (2013) suggest that their distances lie between 4 and 9 kpc, with the mean of 7.4 kpc and the standard deviation of 1.4 kpc. Therefore, these 16 T2C stars, as well as the majority of our variables may lie not exactly in the MWNSC, but just in the inner Galactic bulge.

Besides the single pulsating stars, the unclassified variables could also be eclipsing and ellipsoidal binaries. Due to the range of stellar parameters of their components, the potential eclipsing binaries could distribute widely in the CMD. Ellipsoidal binaries with a giant star component are proposed to explain the 'E' sequence in the period-magnitude diagram of variable stars identified in the Large Magellanic Cloud (Pawlak et al. 2014, and reference therein). Their periods span from 10 d to nearly 300 d. The variability is caused by the deformed atmosphere of the giants, since they fill the Roche lobe. According to the CMD, the stars could not only be RGB stars, but also even dimmer RC stars (Pawlak et al. 2014). Actually, as shown in the CMD of the bottom panel of Fig. 2, a significant number of our variables indeed fall in the region occupied by the RC and RGB stars in the GC.

Confusion with nearby stars with high relative proper motion could also broad the light distribution and cause variability among years. This situation needs to satisfy three requirements: 1) two nearby stars are close by less than one WFC3/IR pixel, so that 'DOLPHOT' package does not disentangle them as two sources; 2) they have similar brightness, for example, less than 2.5 mag difference; 3) they have large relative proper motion (> 127 km s^{-1}, which cause at least one tenth WFC3/IR pixel shift at four-year baseline). We used the proper motion and K-band magnitude information given in Schödel et al. (2009) to examine the impact of confusion on our variable catalog. Schödel et al. (2009) use the *VLT*/NACO dataset in the central $\sim 40'' \times 40''$, which are deeper enough to provide the proper motion of stars 2.5 mag dimmer than the 50% completeness limit of our *HST* dataset in the same field. Fig. 23 gives the fraction of stars, which have counterparts which satisfy the three require-

ments above. The fraction is close to 10% near Sgr A*, but decreases to less than 2% at 23″ away. If we multiple the fraction with the real detected sources in our *HST*/WFC3 dataset, we expect ∼129 variables among the 3268 detected sources, while we find 403 variables. Considering that the confusion effect decreases with the galactocentric radii, we expect no more than 5% of our variable catalog are due to confusion.

6. Summary

We conducted a stellar variability study, based on a set of *HST*/WFC3 IR observations of the Milky Way nuclear star cluster, which consist of 290 dithered exposures taken from years 2010 to 2014. This study bridges the similar works based on large field-of-view surveys obtained with small (< 4m) telescopes and those on high-spatial-resolution adaptive-optics images from ≥ 8 m telescopes. The stable PSF and accurate photometric zeropoints of the *HST* observations enable us to not only provide light curves with much improved accuracy for such known variable stars as E60 (Pfuhl et al. 2014), but also to identify many new variable sources. We have further compared our detected sources with previous variability studies of the Galactic Centre and have made tentative classifications for various sources, individually or statistically, based on their spectroscopic and magnitude/colour properties. Our results are summarized below.

- In total, we detect ∼33,000 sources in the central ∼ 2.3′×2.3′ field. 3894 of them are detected as variable stars, 76 of which show evidence for intraday variability. We have calculated the periods of 36 of these 76 stars.

- Our detection recovers most of the bright variable stars, such as Miras and massive eclipsing binaries. Some variable stars, as identified by Ott et al. (1999), Peeples et al. (2007) and Rafelski et al. (2007) are missed by us probably because 1) underestimated measurement errors, which are most likely systematic, in these studies, and cause mis-identification of non-variable stars; 2) inadequate temporal sampling of the *HST* observations; and 3) the poor resolution of *HST* WFC3 IR camera, leading to severe source confusion in the central few arcseconds field.

- 319 of our detected variables have spectroscopic counterparts, which include WR stars, OB stars, supergiants, Miras and giants.

- For the first time, we have discovered δ Scuti, RR Lyrae Type ab and BL Her stars toward the Galactic Centre.

- The majority of the remaining could be eclipsing/ellipsoidal binaries and Type II Cepheids.

These results demonstrate the power of using *HST*/WFC3 near-IR observations to study variable stars in the Galactic Centre. However, the sampling of current observations is too poor to type stars with variability periods > 2 d. Similar WFC3 observations with optimal cadences are highly desirable for us to accurate derive the periods, classify their types and derive the SFR of the MWNSC at different epoch periods. Such observations do not need to be deep, because the detection is largely limited by the source confusion.

Acknowledgments

We thank the anonymous referee for a thorough, detailed, and constructive commentary on our manuscript. The research leading to these results has received funding from the European Research Council under the European Union's Seventh Framework Programme (FP7/2007-2013) / ERC grant agreement n [614922]. The work is also supported by NASA via the grant AR-14589, provided by the Space Telescope Science Institute. F N-L acknowledges financial support from a MECD predoctoral contract, code FPU14/01700. This work uses observations made with the NASA/ESA Hubble Space Telescope and the data archive at the Space Telescope Science Institute, which is operated by the Association of Universities for Research in Astronomy, Inc. under NASA contract NAS 5-26555. We are grateful to Zhiyuan Li, Francisco Najarro, Jon Mauerhan, Stephen Eikenberry and Farhad Yusef-Zadeh for many valuable comments and discussion. We also want to thank Siro Benvenutto Gallego, the son of Eulalia Gallego-Cano to help us visually identify variable stars.

A. Photometric Uncertainty

Uncertainty (σ_v) is a key element in the least chi-square method in §3 to identify variable stars. If we over- or underestimated the uncertainty, we would miss the real variable stars or detect too many variable stars. In this section, we will use the real dataset to judge the photometric uncertainty estimated from the artificial star tests.

If we assume that most of detected stars are non-variable, the median value of the standard deviation of magnitudes from individual dithered exposures of stars in different magnitude and local surface brightness bins could be a good representative of σ_v. The top panel of Fig. 24 shows the standard deviation for individual stars (black dots) and their median values as a function of the F153M magnitude (green diamonds). For each magnitude

bin, the large scatting of the standard deviation (black dots) is due to the variation of local surface brightness. The median value (green diamonds) is roughly 0.03 mag for stars with F153M<17 mag and then increases with the F153M magnitude. In the bottom panel, we compare the relationship between the median values of the standard deviation and the F153M magnitude for dithered exposures at different periods. The relationship at individual periods (dotted lines with different colours) are very similar, median standard deviation is ∼0.01 mag for F153M<17 mag and then increases with the magnitude. However, the median standard deviation at each magnitude bin increases with the duration of the dithered exposures; first all the observations in 2014, then those in 2010 and 2011, 2011 and 2012, or 2012 and 2014. The median standard deviation derived from all the dithered exposures from 2010 to 2014 are the largest. The shift of the median standard deviation at different combination of dithered exposures seems to be independent to the magnitude and could be a systematic error.

We want to understand the temporal evolution of the median standard deviation shown in the bottom panel of Fig. 24: 0.01 mag error for the single epoch and ∼0.025 mag for the whole dateset. Several factors could contribute the detected error: 1) Poisson statistic error due to the electrons. This error is very tiny for the bright stars and is independent on observation time. Therefore, Poisson statistic error is not the solution; 2) The temporal variation of the photometric zeropoint keyword ('PHOTFLAM'). This keyword is used to translate the image units (electron/s) into astrophysics units (such as Vega magnitude). The homepage of WFC3[12] mentions ∼1% uncertainty in PHOTFLAM from the calibration programs. The differences between PHOTFLAM among different dithered exposures could cause a systematic error in the observed magnitude. However, we do not expect a variation of PHOTFLAM in each period with duration as less than 0.3 hours (Group 4 in Table 1) to explain the 0.01 magnitude error of bright stars in the single epoch. We also try to derive the median magnitude correction of dithered exposures in 2010, 2011 and 2014, with respect to the 2012 observations. The correction is very small <0.01 mag. Even we correct this value, the median standard deviation for dataset with four-year baseline are only slightly reduced; 3) The uncertainty on the flat-fielding calibration files. The above result suggests that the photometry correction could change spatially. At different dithered exposures, the same source could fall into different locations of the instrument. The uncertainty on the instrument response (i.e. the flat-fielding calibration) could introduce a systematic error. Dahlen (2013) suggest a 0.7% error for the flat-fielding uncertainty. This value could probably explain the 0.01 mag in the single epoch, but not the extra 0.02 mag difference between single epoch and multiple epochs; 4) WFC3/IR intra-pixel sensitivity. If the centroid of the PSF falls into the gaps between pixels, its total flux reduces, which is known as 'intra-pixel sensitivity

[12]http://www.stsci.edu/hst/wfc3/phot_zp_lbn

variation'. For an undersampling instrument, likes WFC3/IR, this effect is more significant in the short wavelength. Pavlovsky et al. (2011) suggests a 0.44% uncertainty due to the 'intra-pixel sensitivity variation' in the F160W band (1.53 μm). Therefore, it still cannot completely solve our problem; 5) PSF fitting on the undersampling detector. The FWHM of the WFC3/IR PSF at 1.5 μm[13] is only 1.136 WFC3/IR pixels. All our observations use a coarse half-pixel dithering, making accurately determination of the stellar centroid very hard. Therefore, an error on the stellar centroid from the mosaic image could introduce a systematic uncertainty on the photometry determined from individual dithered exposures through the PSF fitting. For observations within short period, the relatively astrometry between dithered exposures could be determined accurately. Therefore, they suffered from the same systematic uncertainty introduced by the PSF fitting. Instead, observations at long period, with different pointing and rotation angles, they could suffer different systematic uncertainty, which in turn is transferred into the median standard deviation. In summary, the flat-fitting uncertainty and WFC3/IR intra-pixel sensitivity contribute 0.01 mag error in the single epoch, while the PSF fitting on the undersampling detector and the temporal variation of 'PHOTFLAM' contribute an extra 0.015 mag error among multiple epochs.

Figure. 25 compares the median standard deviation from the observation and the artificial star test, but with different methods: 1) the photometric uncertainty, σ_{F153M} (black dotted line), which is the square root of the quadratic sum of the systematic and the statistic parts, i.e. the median absolute value and 68% percentiles of the difference between the output and the input magnitudes ; 2) standard deviation of output magnitudes of the dithered exposures (σ_v); 3) photometric uncertainty ($\sigma_{DOLPHOT}$) output by the 'DOLPHOT' package, which only considered the Poisson uncertainty. We also add 1% and 2.5% systematic uncertainty into the median standard deviation derived from the second and third methods above. We can see that σ_{F153M} seriously overestimate the observed median standard deviation for stars brighter than >16 mag in the F153M band. Instead, σ_v, plus 1% and 2.5% systematic error match the observed median standard deviation for single epoch and multiple epochs, very well to magnitudes ∼20.5 mag. Beyond that, $\sigma_{DOLPHOT}$ fits the observed one better.

B. Variability among Dithered Exposures

We found that there is a correlation between the phenomenon, i.e., quick intensity variation among dithered exposures, and the 'CHI' quality parameter. For each source, we defined the $\overline{CHI}$ as the mean 'CHI$_i$' of dithered exposures in Groups 5 to 7 in Table 3, the

[13]http://www.stsci.edu/hst/wfc3/documents/handbooks/currentIHB/c07_ir07.html

dithered exposures in which are used to derive χ^2_d too. The top panel of Fig. 26 shows the distribution of $\overline{CHI}$ for our sources. The peak of the distribution centered on 1.3 and 68% percentile is [0.73,2.66]. The bottom panel of Fig. 26 gives the fraction of stars with $\chi^2_d > 2.42$ (the upper 90% percentile of the χ^2_d for all the sources are [0.58,2.42]) as a function of $\overline{CHI}$ (the bottom panel). We can see that the fraction of short variable stars increases, even the number of stars decreases. Considering that the majority of stars with large $\chi^2_d > 2.42$ suffer from the artificial mentioned above, we believe that this artificial is strong correlated with the 'CHI' parameter. As a result of the bad PSF fitting, the uncertainty of the center position introduced by the dithering patterns artificially produced a regular variability among dithered exposures.

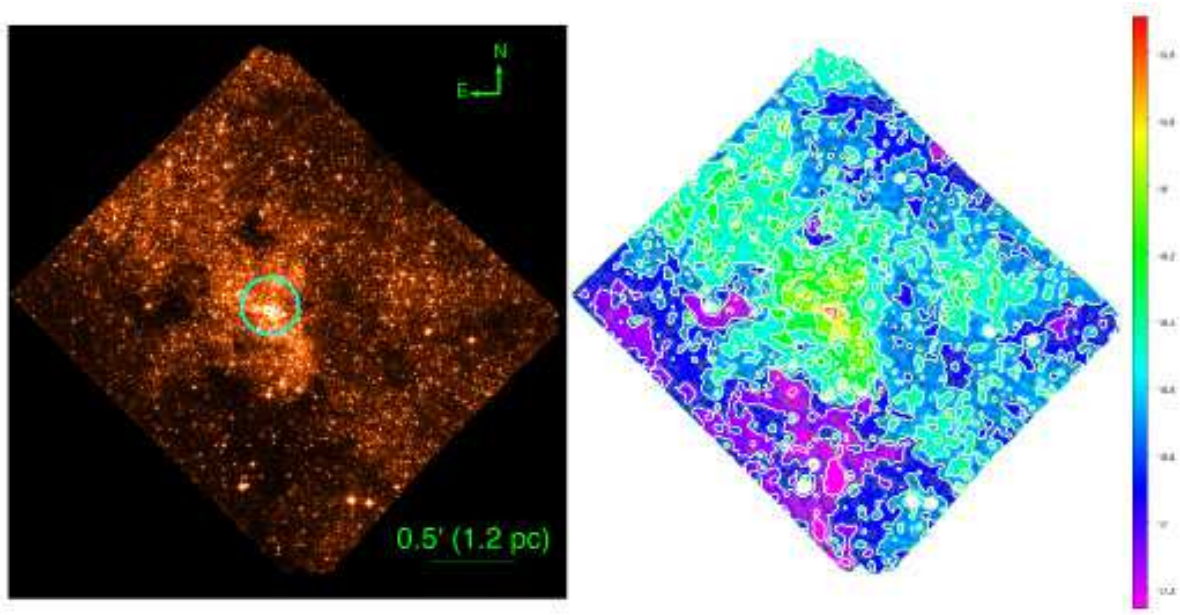

Fig. 1.— Left: *HST*/WFC3 F153M observations of the MWNSC. The cyan circle indicates a radius of 10 arcseconds around Sgr A*. High extinction regions with low stellar number densities can easily be recognized. Right: the spatial distribution of the logarithm of the smoothed surface brightness (in units of ergs s^{-1} cm^{-2} $Å^{-1}$ $arcsec^{-2}$). The white contours divide the image into ten regions with the surface densities defined in Table 2.

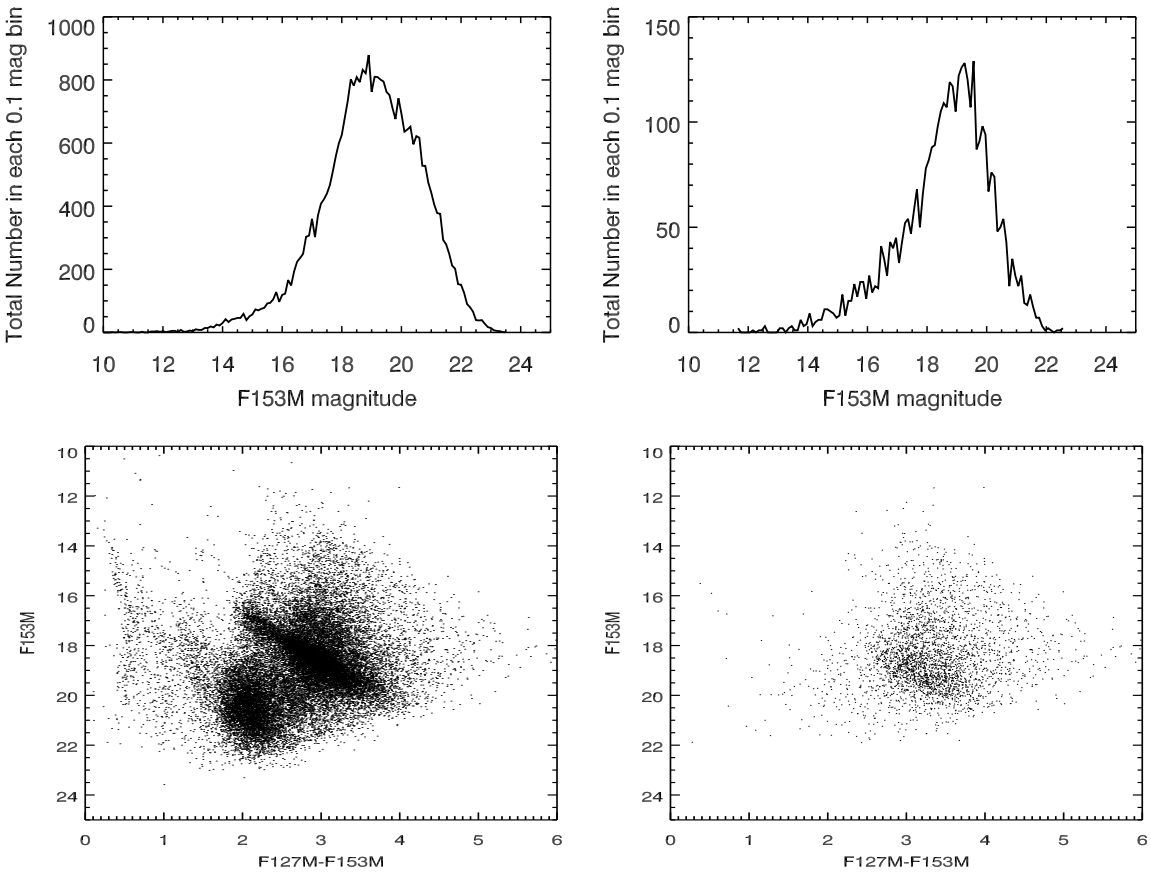

Fig. 2.— Top panels: the F153M magnitude distribution of all detected sources (left) and variable candidates (right). Bottom panels: the colour-magnitude diagram (F127M-F153M vs. F153M) of the detected sources (left) and variable candidates (right).

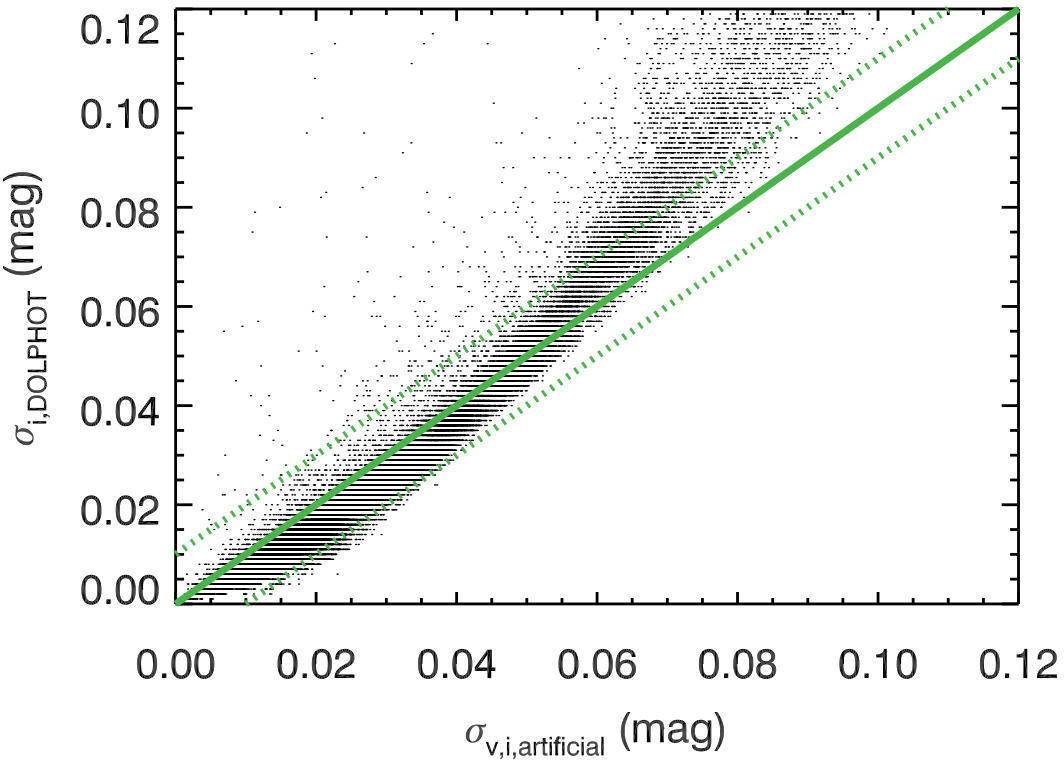

Fig. 3.— Comparison of the $\sigma_{v,i}$ derived by the artificial star tests ($\sigma_{v,i,artificial}$) and the photometric uncertainties from the 'DOLPHOT' ($\sigma_{i,DOLPHOT}$). The solid and dashed lines represent $\sigma_{i,DOLPHOT}$=$\sigma_{v,i,artificial}$ and $\sigma_{i,DOLPHOT}$=$\sigma_{v,i,artificial}$ $\pm$ 0.01, respectively.

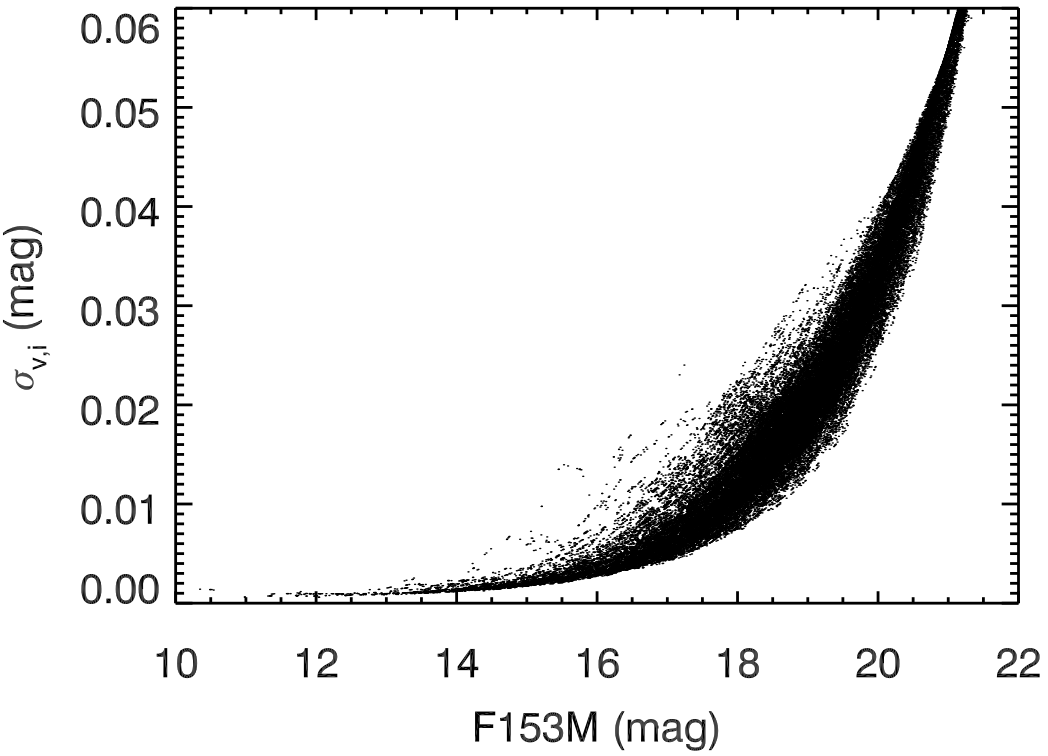

Fig. 4.— The $\sigma_{v,i}$ as a function of the input F153M magnitude.

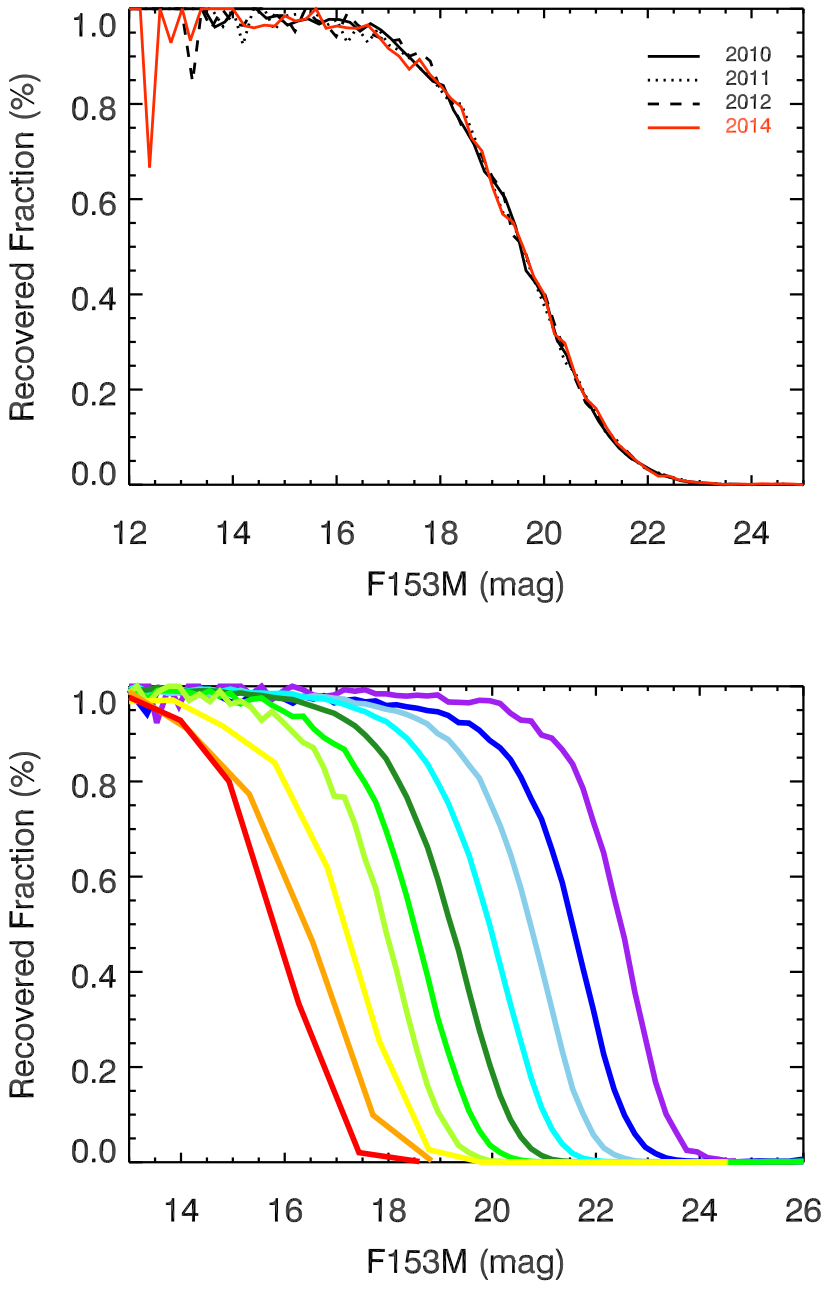

Fig. 5.— The recovered fraction as a function of input F153M magnitude from the artificial star tests for the four different years (top panel) and regions with different surface brightness given in Fig. 1 (bottom panel). In the bottom panel, from left to right, the regions indicated by the solid lines with different colours have decreasing surface densities.

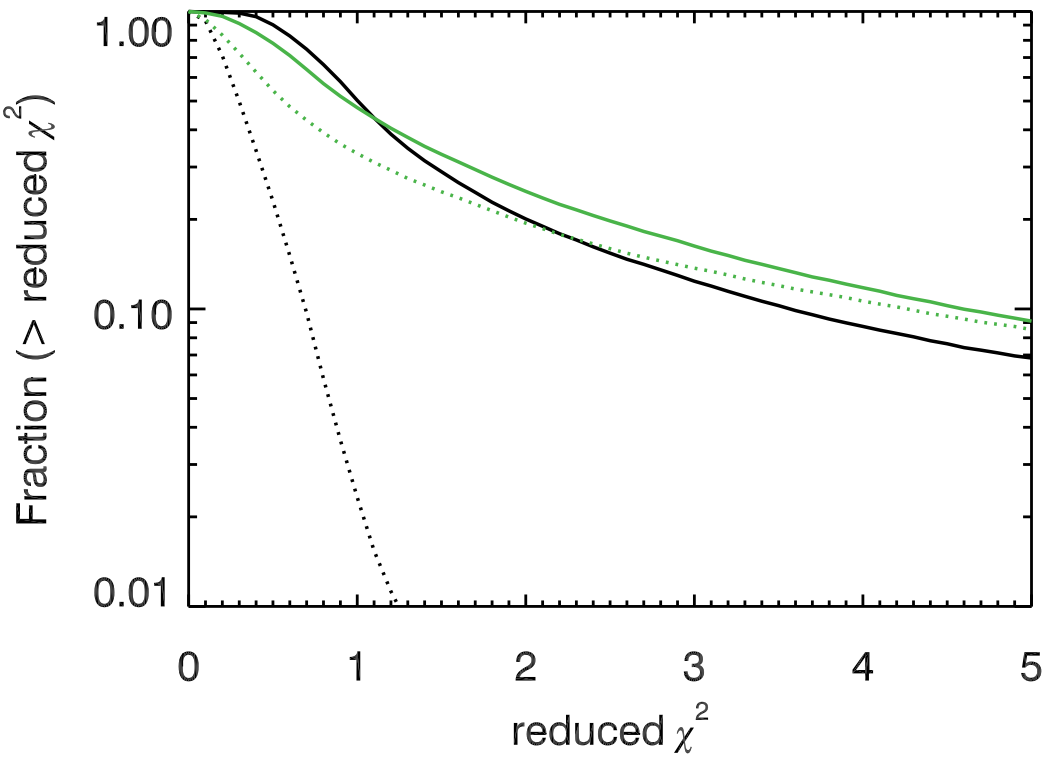

Fig. 6.— The cumulative distribution function (> reduced χ^2) for χ^2_y (green solid line), χ^2_d (green dotted line), $\chi^2_{y,b}$ (black solid line), $\chi^2_{d,b}$ (black dotted line), see §3 for a description of these values.

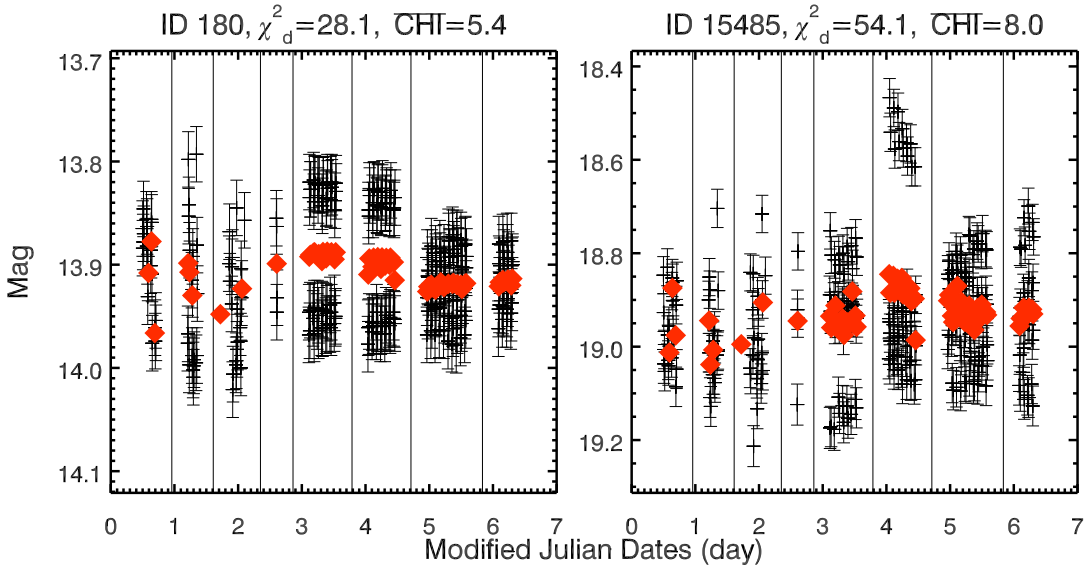

Fig. 7.— The *HST*/WFC3 F153M light curves of two stars with different magnitudes, the variability of which is not considered to be real. The black data points are from the 290 dithered exposures, while the red filled diamonds are the magnitudes after the binning procedures described in §3. The seven vertical lines divide the data points into eight groups as shown in Table 1: The first three groups are observations in 2010, 2011 and 2012, while the last five groups are observations from February to April, 2014. For easy demonstration, a constant has been subtracted from the Julian dates of dithered exposures in each group, so that the modified Julian date of the first dithered exposure in each group is 0.5 day later than the last dithered exposure in the previous group. In the title of each figure, we give the source ID, χ^2_d as defined in §3, and $\overline{CHI}$ defined in Appendix B.

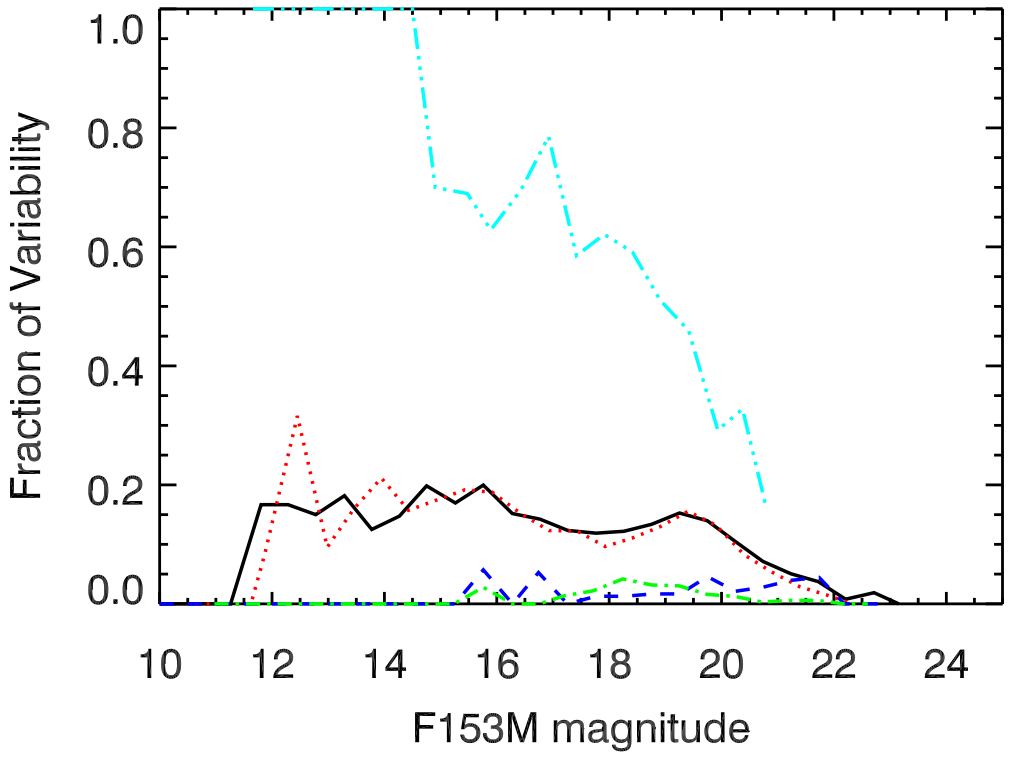

Fig. 8.— The fraction of variable stars as a function of the F153M magnitude. The black solid line: all stars, blue dashed: stars with F127M-F153M<1.7 (presumably foreground stars), green dash-dot: 1.7<F127M-F153M<2.2 (foreground Galactic bulge), red dotted: 2.2<F127M-F153M<3.8 (GC) and cyan dash dot dot: background or AGB stars in the GC embedded in the interstellar dust.

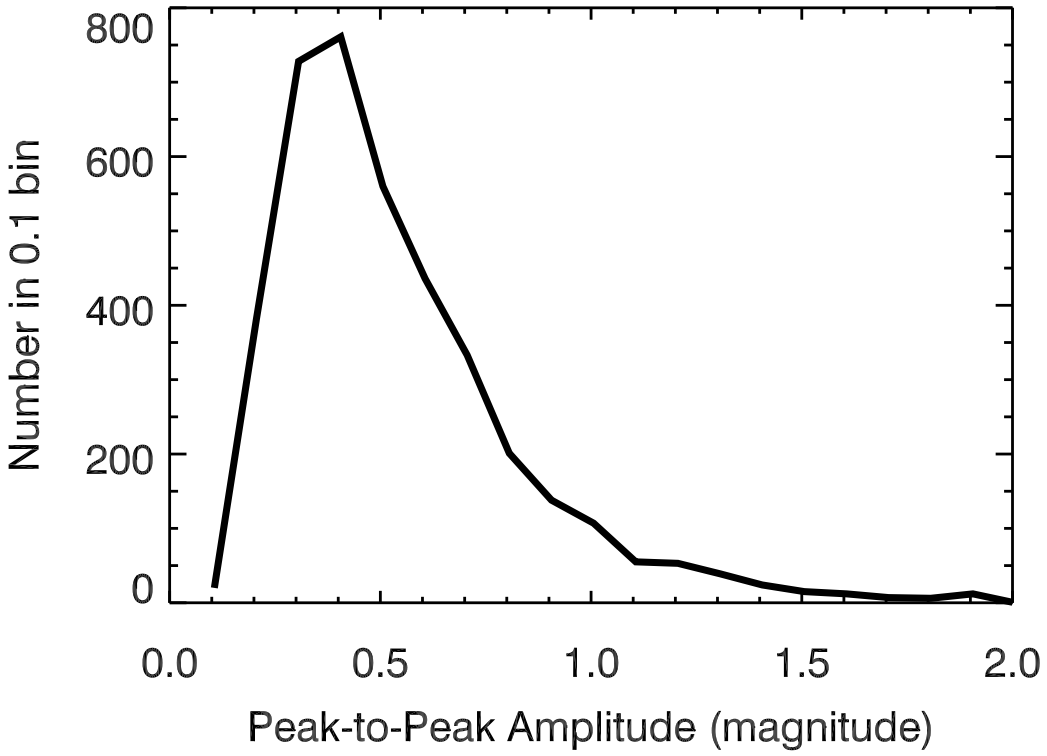

Fig. 9.— The peak-to-peak amplitude distribution of the variable stars.

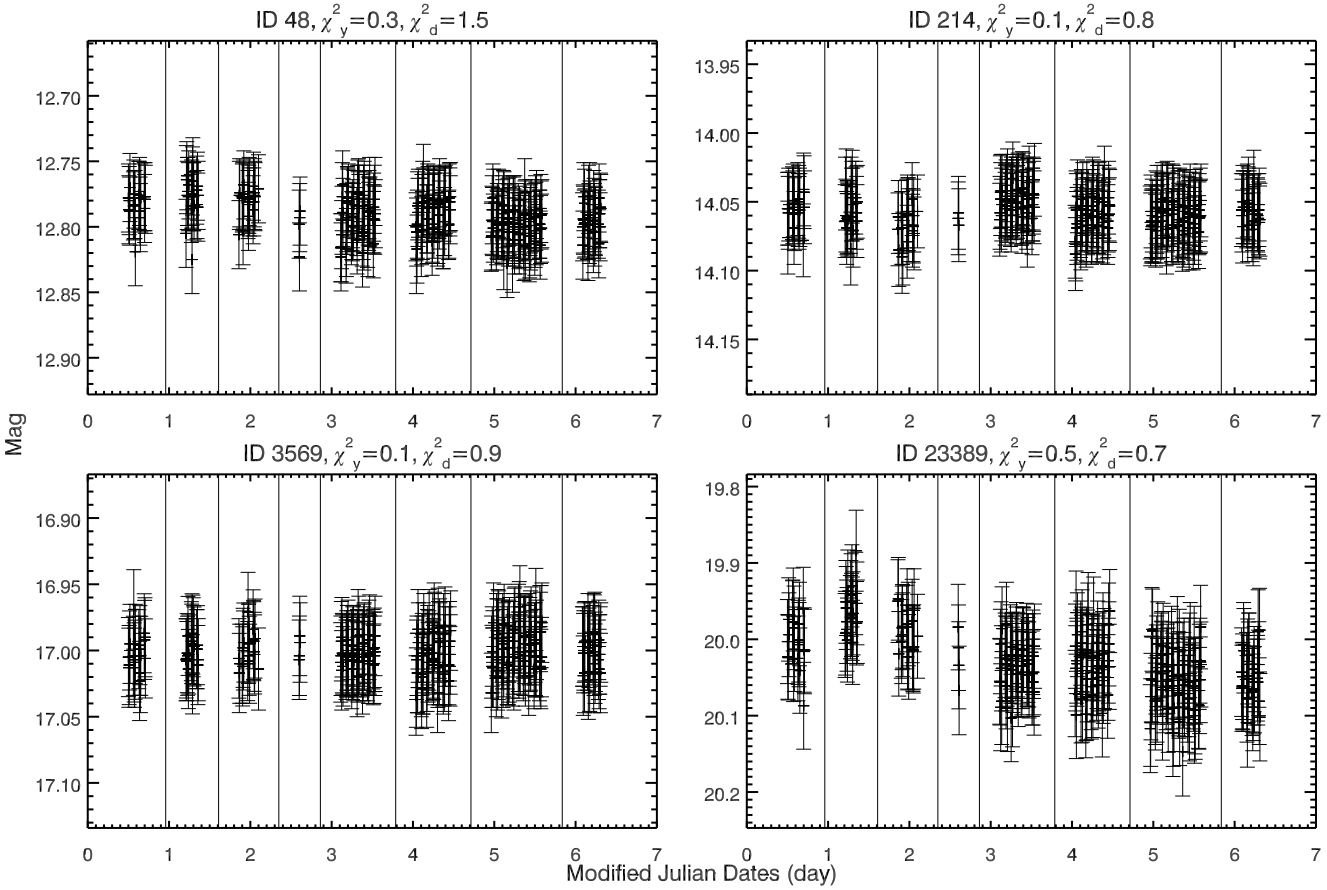

Fig. 10.— The *HST*/WFC3 F153M light curves of four non-variable stars with different magnitudes. The symbols ('pluses' and vertical lines) are the same as those in Fig. 7. In the title of each figure, we give the source ID, χ^2_y and χ^2_d defined in §3.

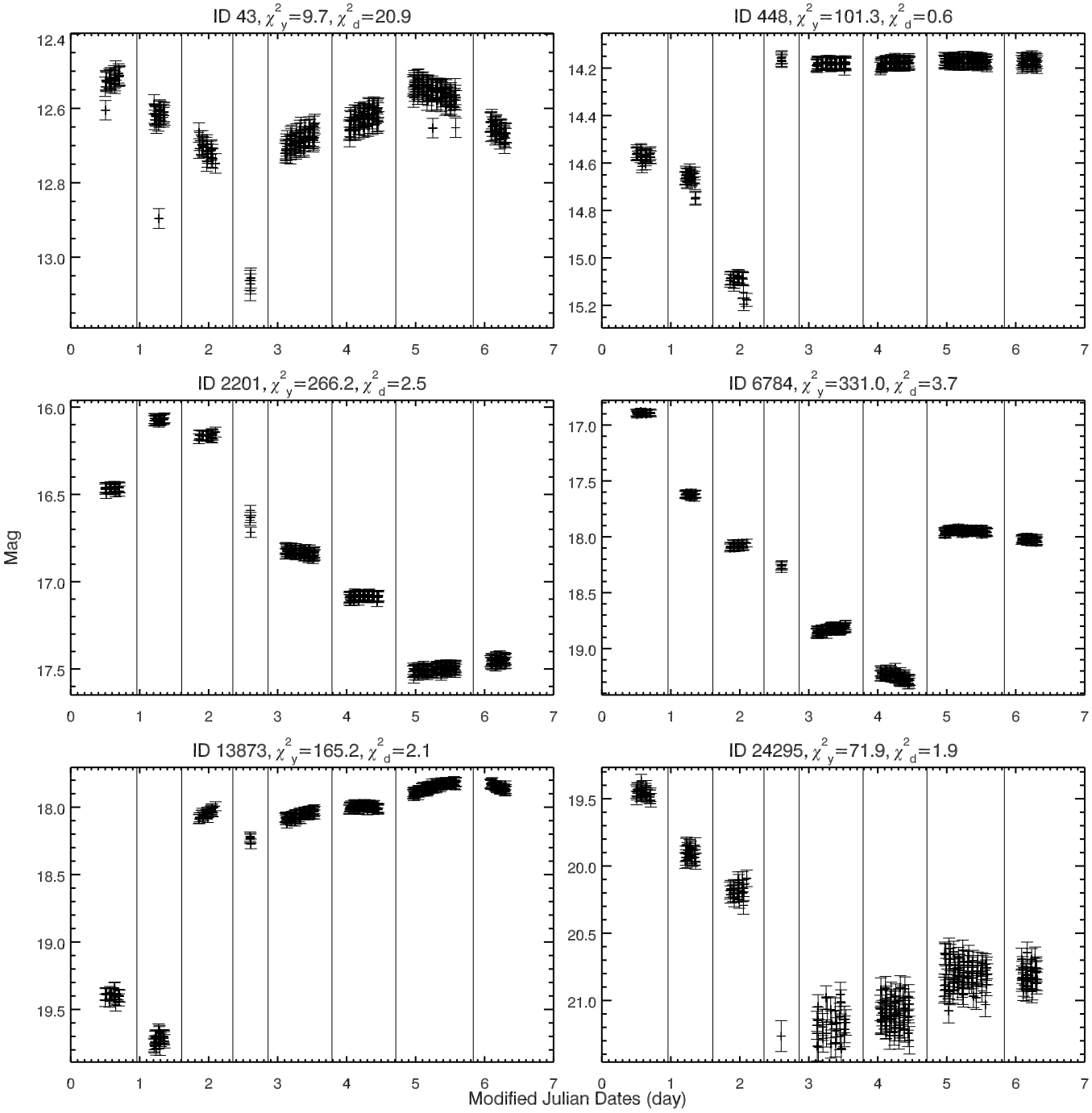

Fig. 11.— The *HST*/WFC3 F153M light curves of four stars with different magnitudes, which are identified to vary on yearly time scales. The symbols ('pluses' and vertical lines) are the same as those in Fig. 7. In the title of each figure, we give the source ID, χ^2_y and χ^2_d, as defined in §3.

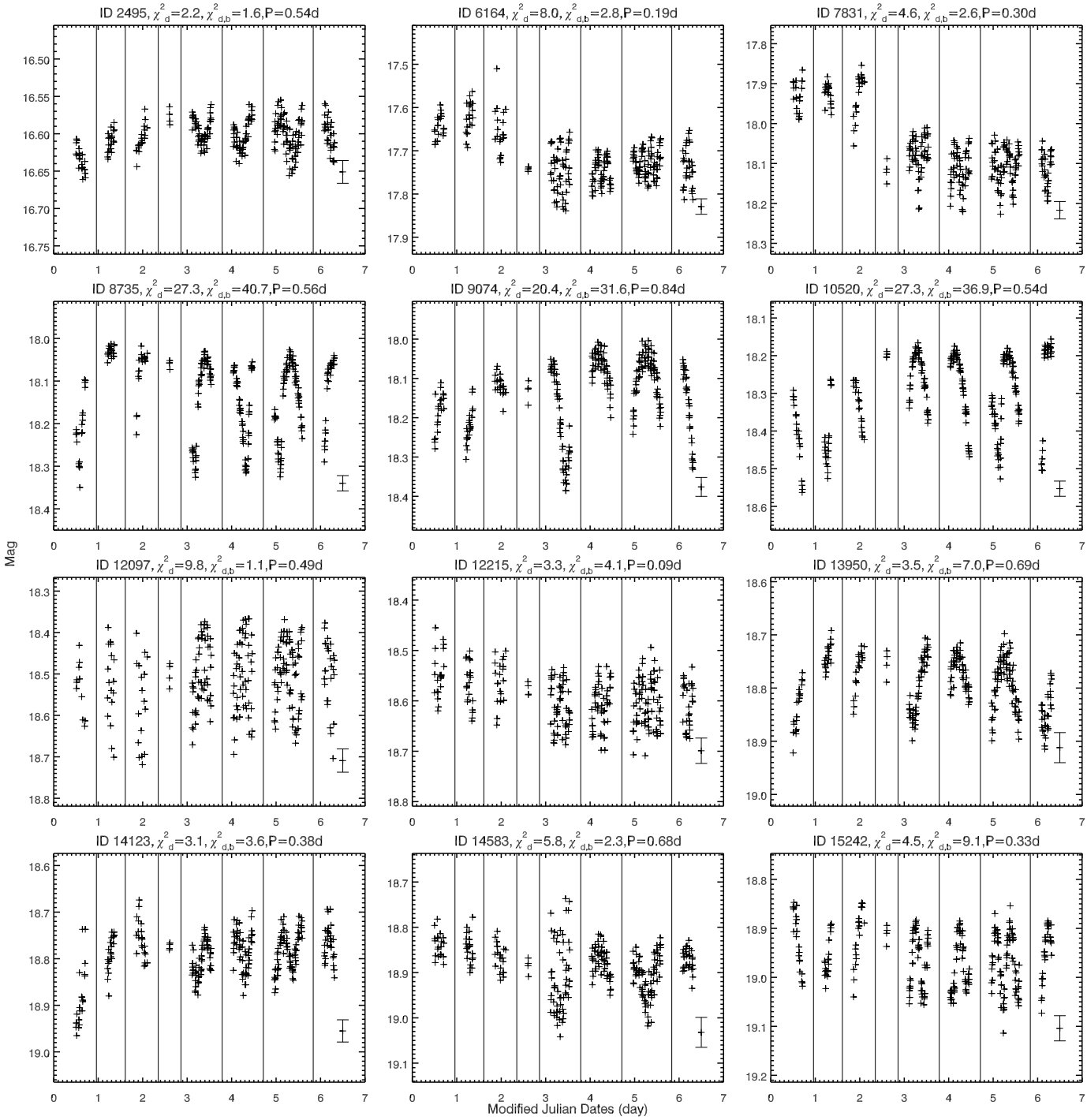

Fig. 12.— The *HST*/WFC3 F153M light curves of 28 sources with measured periods. The vertical lines are the same as those in Fig. 7. The error bar in the lower right corner of each panel represents the average uncertainty. In the title of each panel, we give the source ID, χ^2_d and $\chi^2_{d,b}$, as defined in §3, as well as the periods calculated in §4.

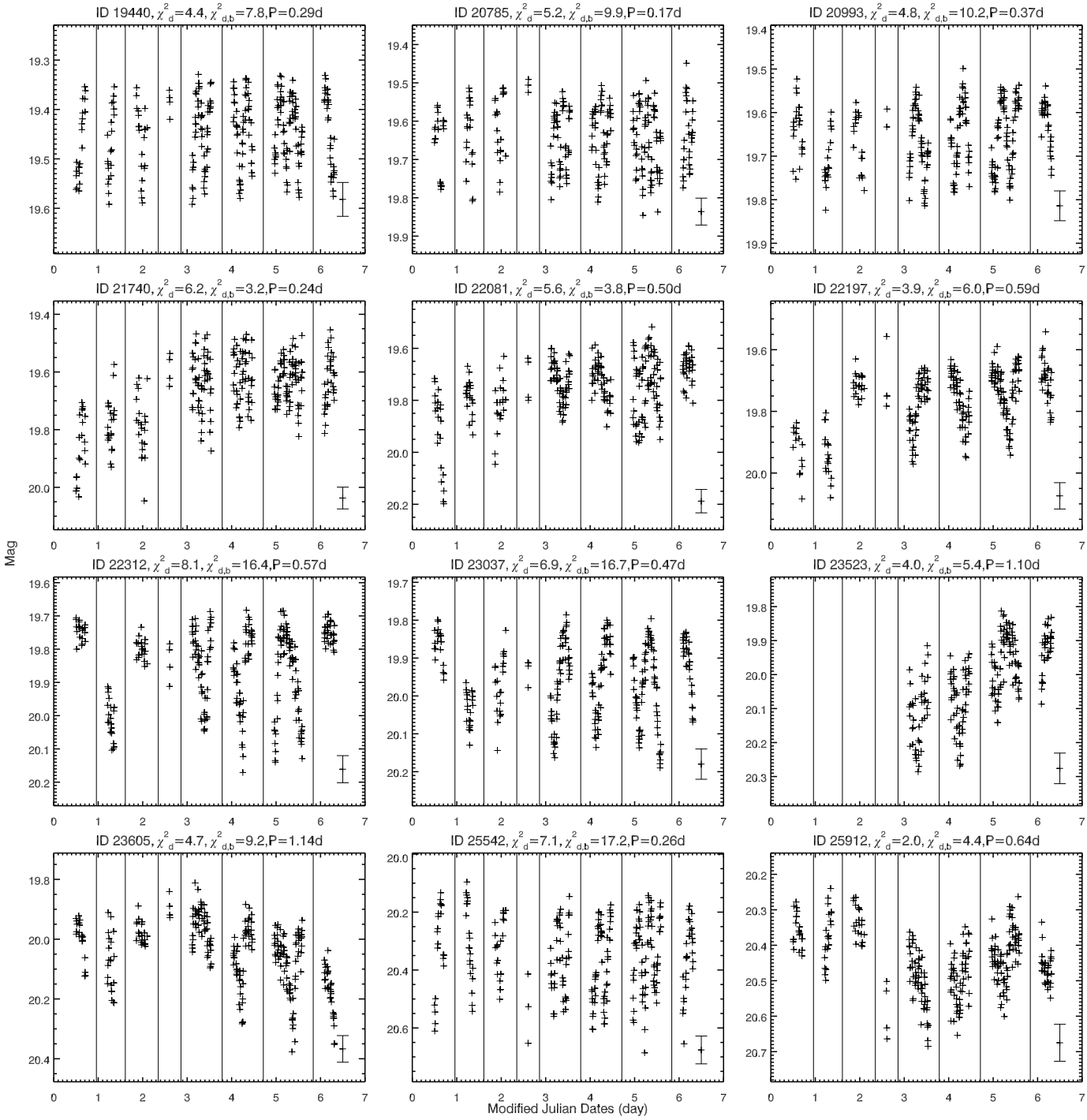

Fig. 13.— Continued Fig. 12.

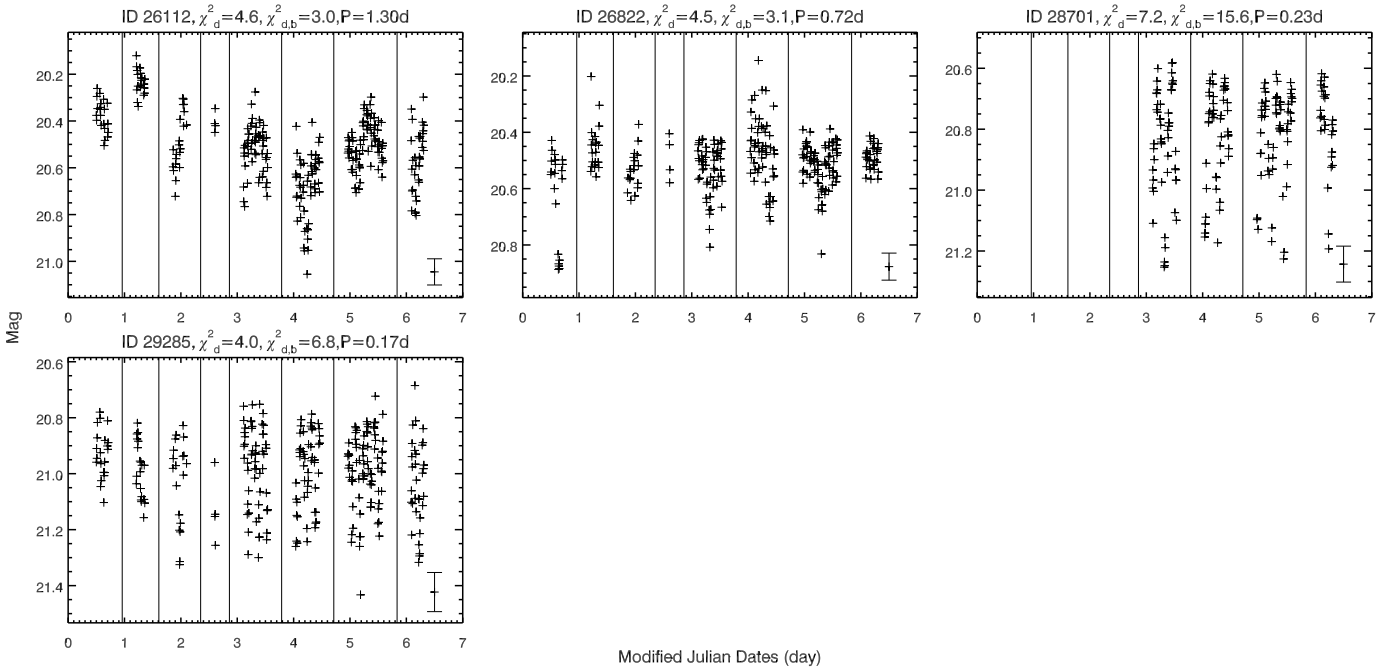

Fig. 14.— Continued Fig. 12.

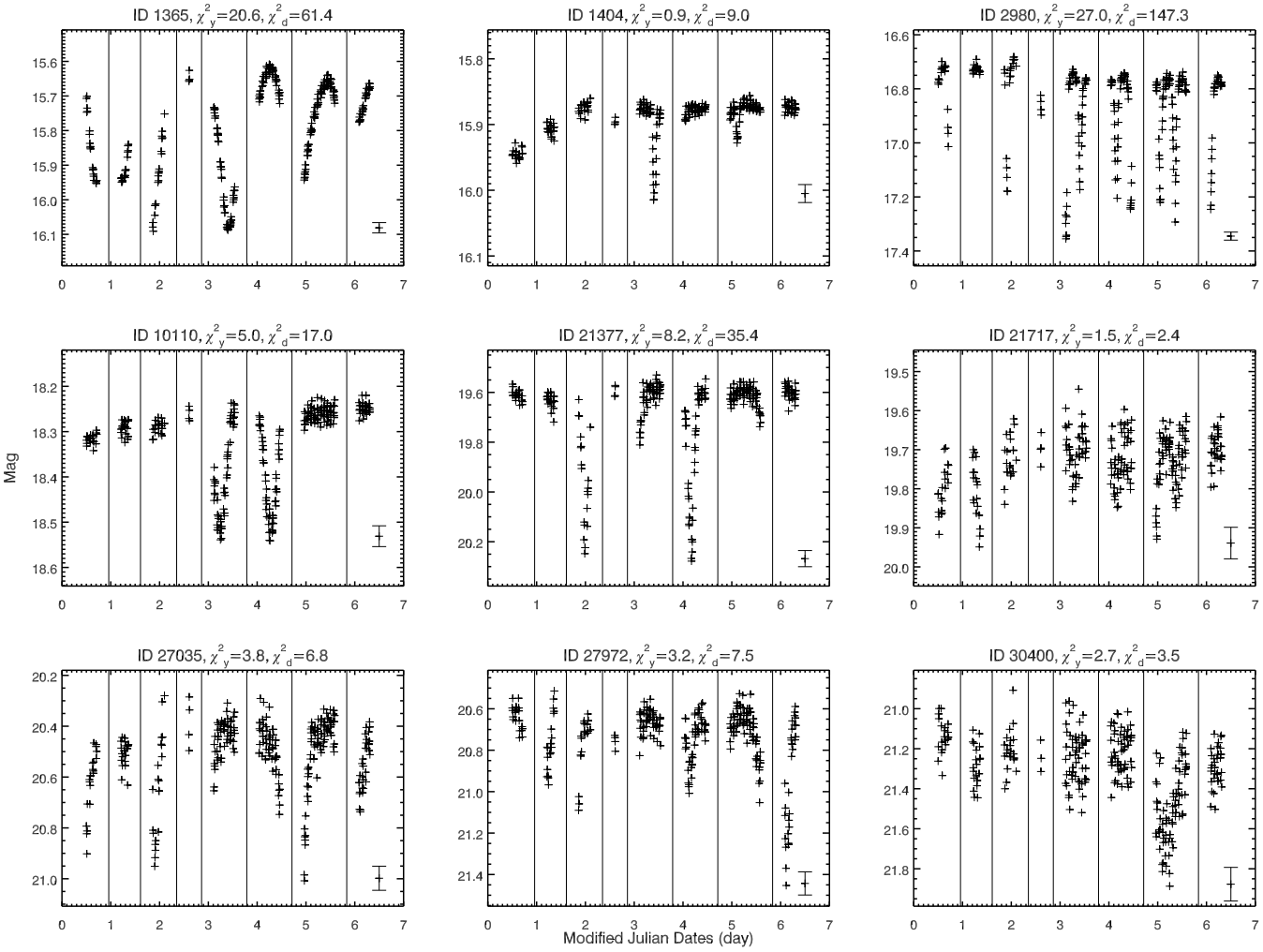

Fig. 15.— The *HST*/WFC3 F153M light curves of nine eclipsing binary candidates. The vertical lines are the same as those in Fig. 7. The error bar in the lower right corner of each panel represents the average uncertainty. In the title of each figure, we give the source ID, χ^2_y and χ^2_d, as defined in §3.

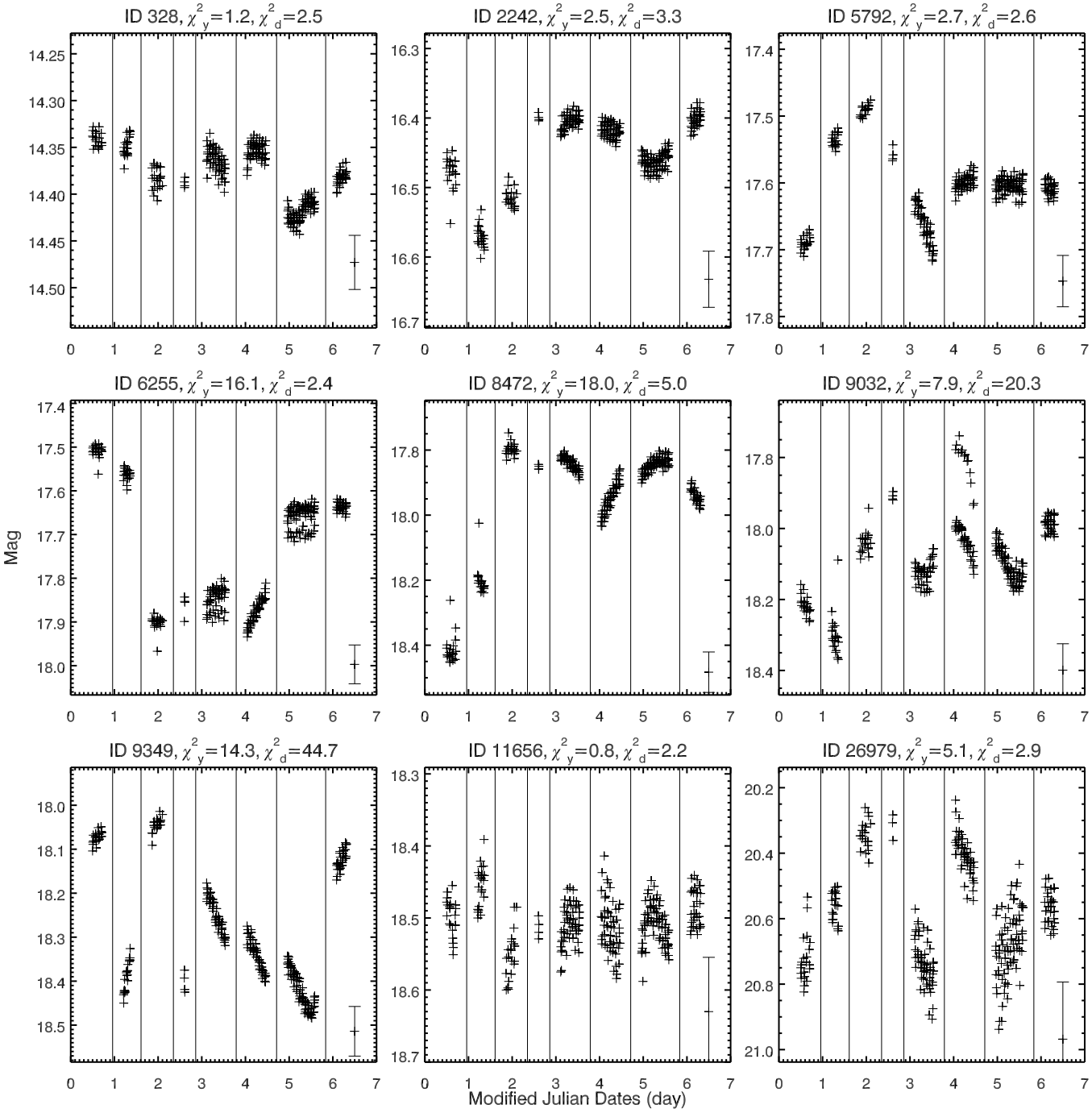

Fig. 16.— The *HST*/WFC3 F153M light curves of nine stars with different magnitudes and intraday variability. The vertical lines are the same as those in Fig. 7. The error bar in the lower right corner of each panel represents the average uncertainty. In the title of each figure, we give the source ID, χ^2_y and χ^2_d, as defined in §3.

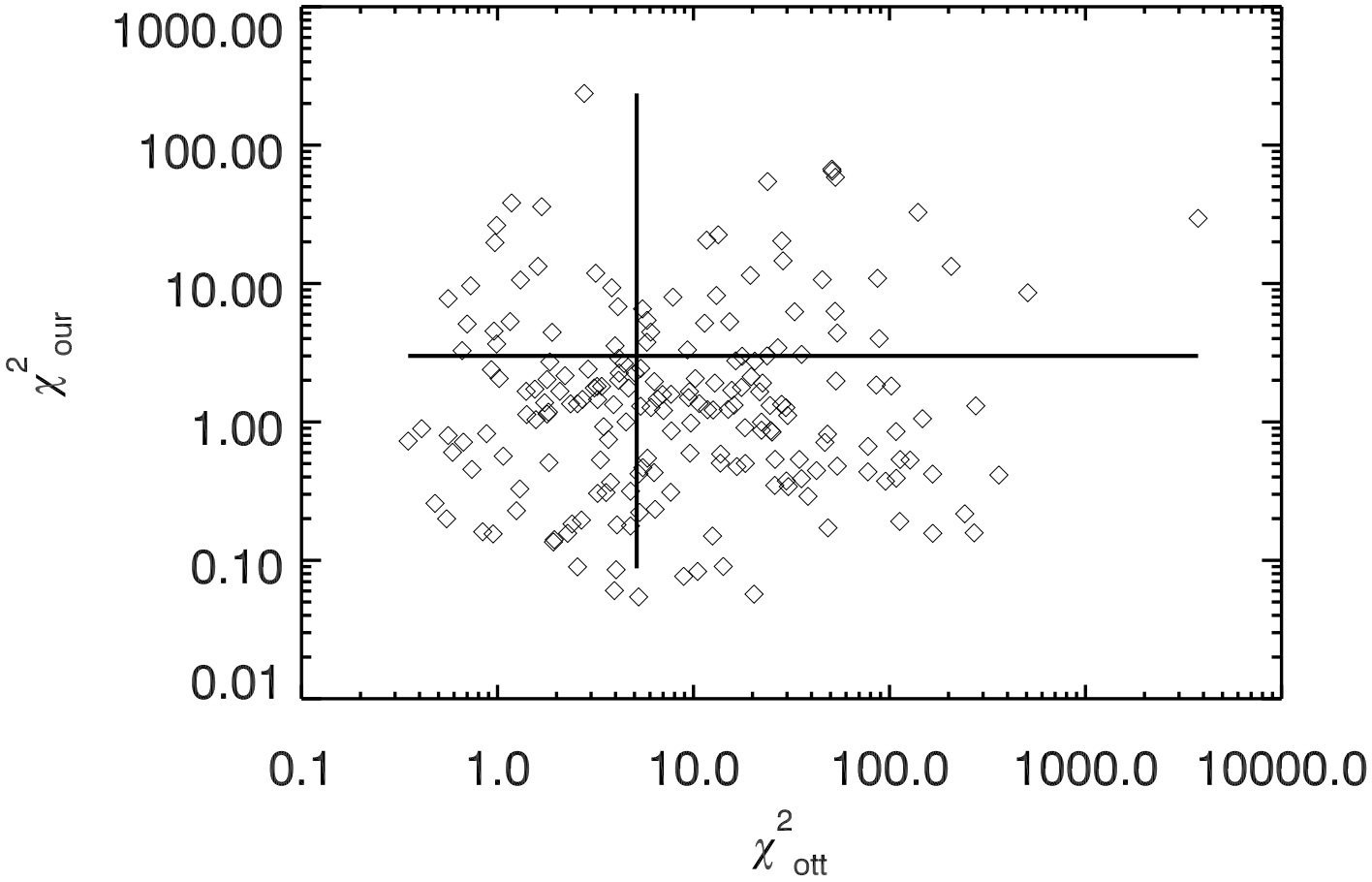

Fig. 17.— Comparison of the reduced χ^2 derived from Ott et al. (1999) (χ^2_{ott}) and our dataset (χ^2_{our}). For each source, χ^2_{our} is the minimum of χ^2_y and $\chi^2_{y,b}$. The vertical and horizontal lines are the cut to separate the variable or non-variable stars: χ^2_{ott}=5.13 from Ott et al. (1999) and χ^2_{our}=3.

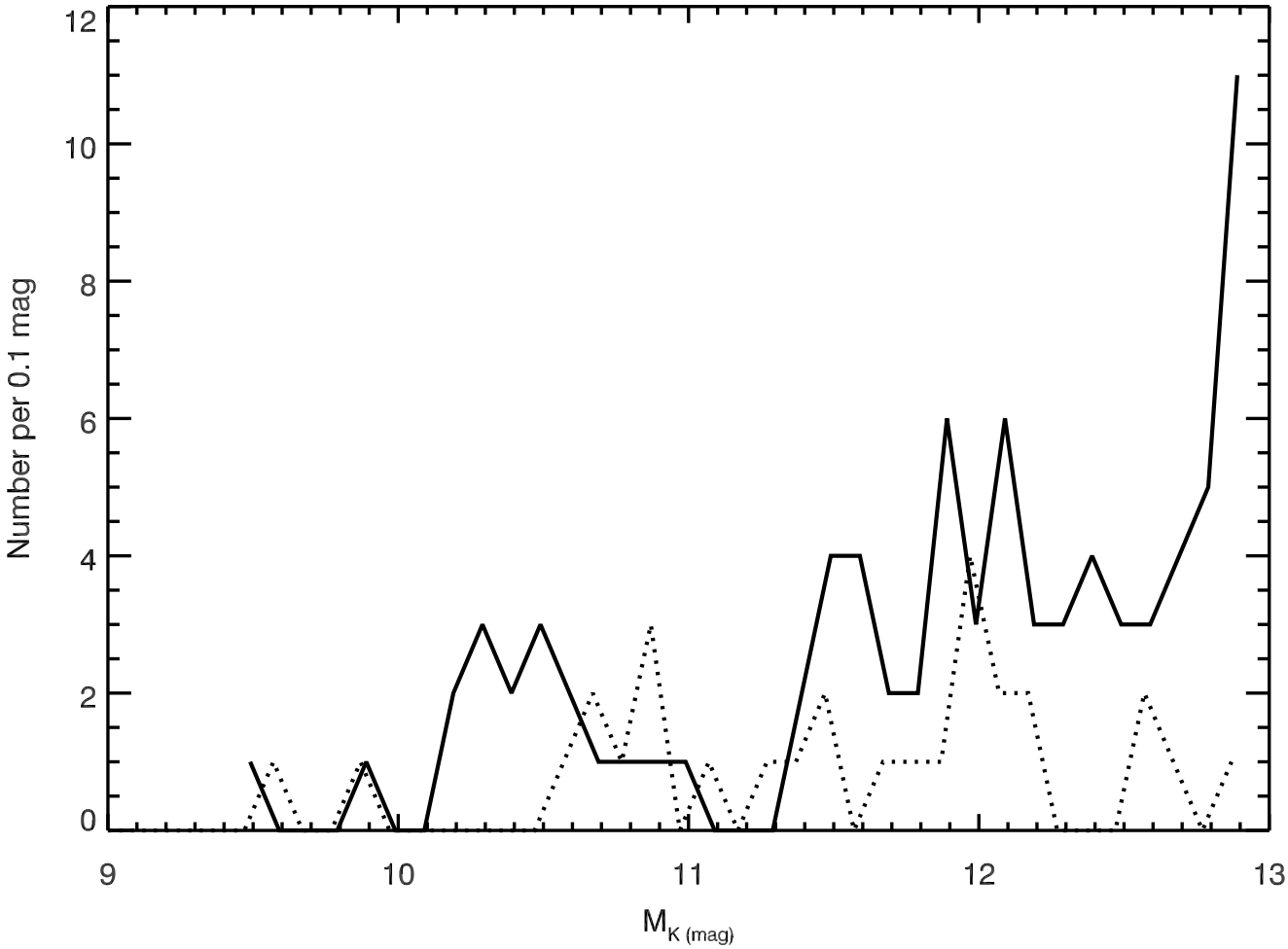

Fig. 18.— The K-band magnitude distributions of variable stars defined in Ott et al. (1999), which are classified as non-variable (solid line) and variable (dotted line) in our dataset.

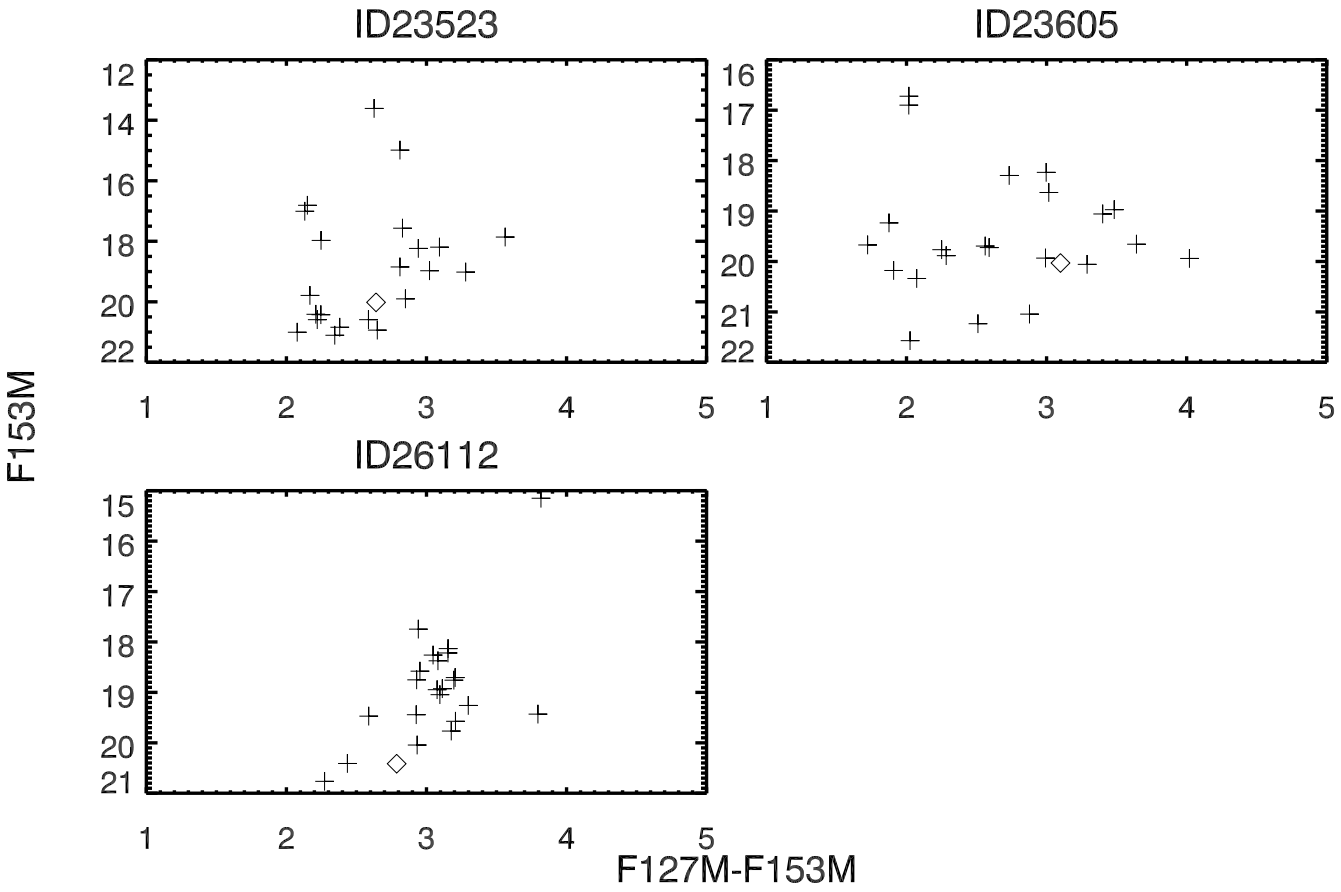

Fig. 19.— The colour magnitude diagrams (F127M-F153M vs. F153M) of the detected sources (pluses) within 2″ of the three T2C candidates (diamonds), the IDs of which are given in the titles.

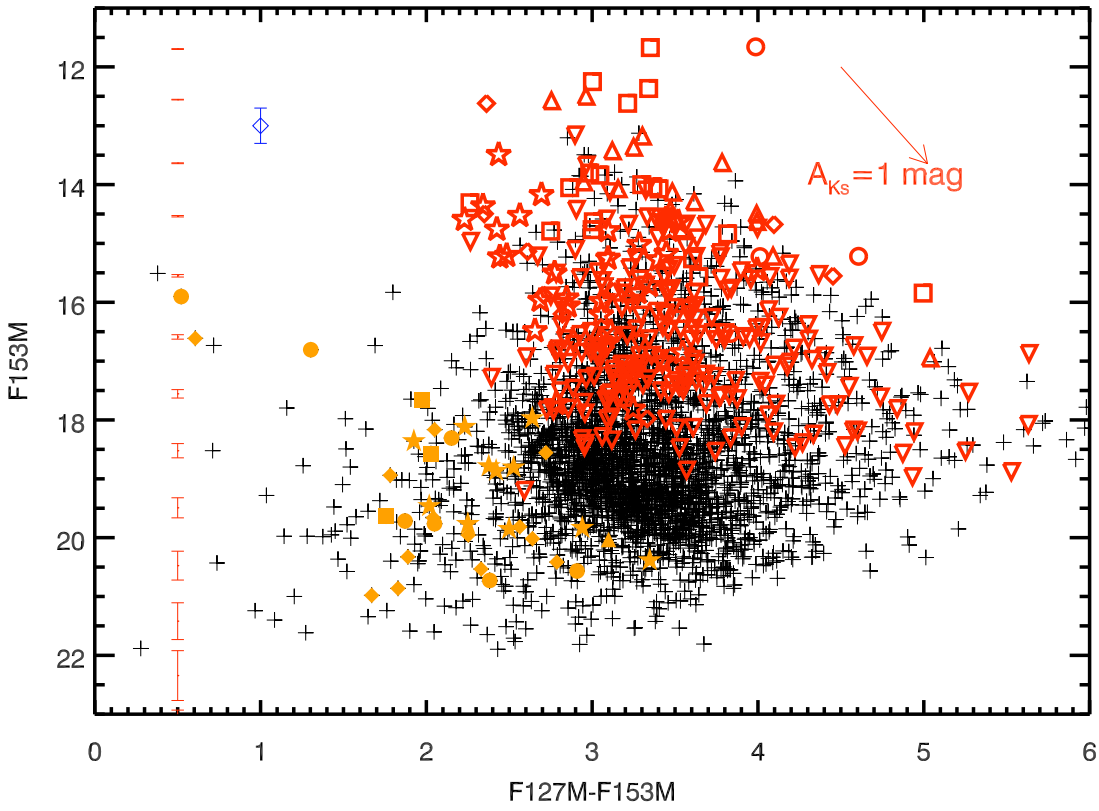

Fig. 20.— Comparison of the CMD of variable stars with spectroscopic identifications (red open symbols), identifications determined from their light curves and periods (yellow filled symbols) and those without available spectroscopic identifications or variable type classification (black plus). Red diamonds represent WR stars, asterisks OB stars, squares Miras (LPVs), circles supergiants ('I' in Blum et al. 2003), triangles giants ('III' in Blum et al. 2003), and downward-pointing triangles other late-type stars. Yellow circles represent eclipsing binaries with well determined periods in §4, squares 3 δ Scuti, stars 11 RRLs, triangles T2Cs and filled diamonds 11 candidates of eclipsing binaries. On the left, the red interval bars are the σ_{F153M} at different F153M magnitudes and the blue diamond with an error bar represents the photometric uncertainty introduced by a 1 kpc error in the distance modulus.

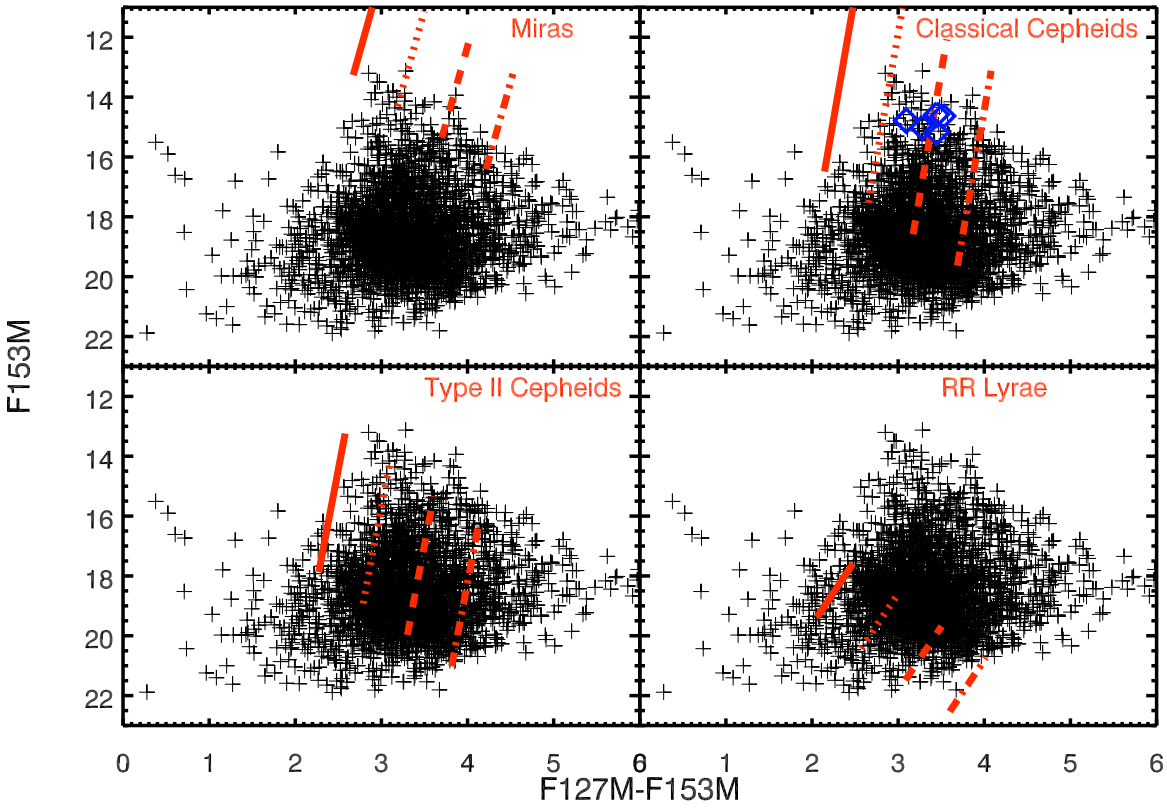

Fig. 21.— Comparison of the CMD of variable stars with the ranges predicted by the period-luminosity functions of variable stars with different types, assuming that they are in the GC. We cannot calculate the period of 99% of our sample in order to classify their variable type, so these ranges are plotted for qualitative purposes only. The solid, dotted, dashed and dot-dashed red lines have been reddened with A_{Ks}=2, 2.5, 3 and 3.5 mag. In the top right panel, the blue diamonds around F127M-F153M∼3.3 mag and F153M∼ 15 mag are five CCEP candidates, which are classified as intermediate-age stars (50 to 500 Myr old) by Nishiyama et al. (2016) and show variability among years.

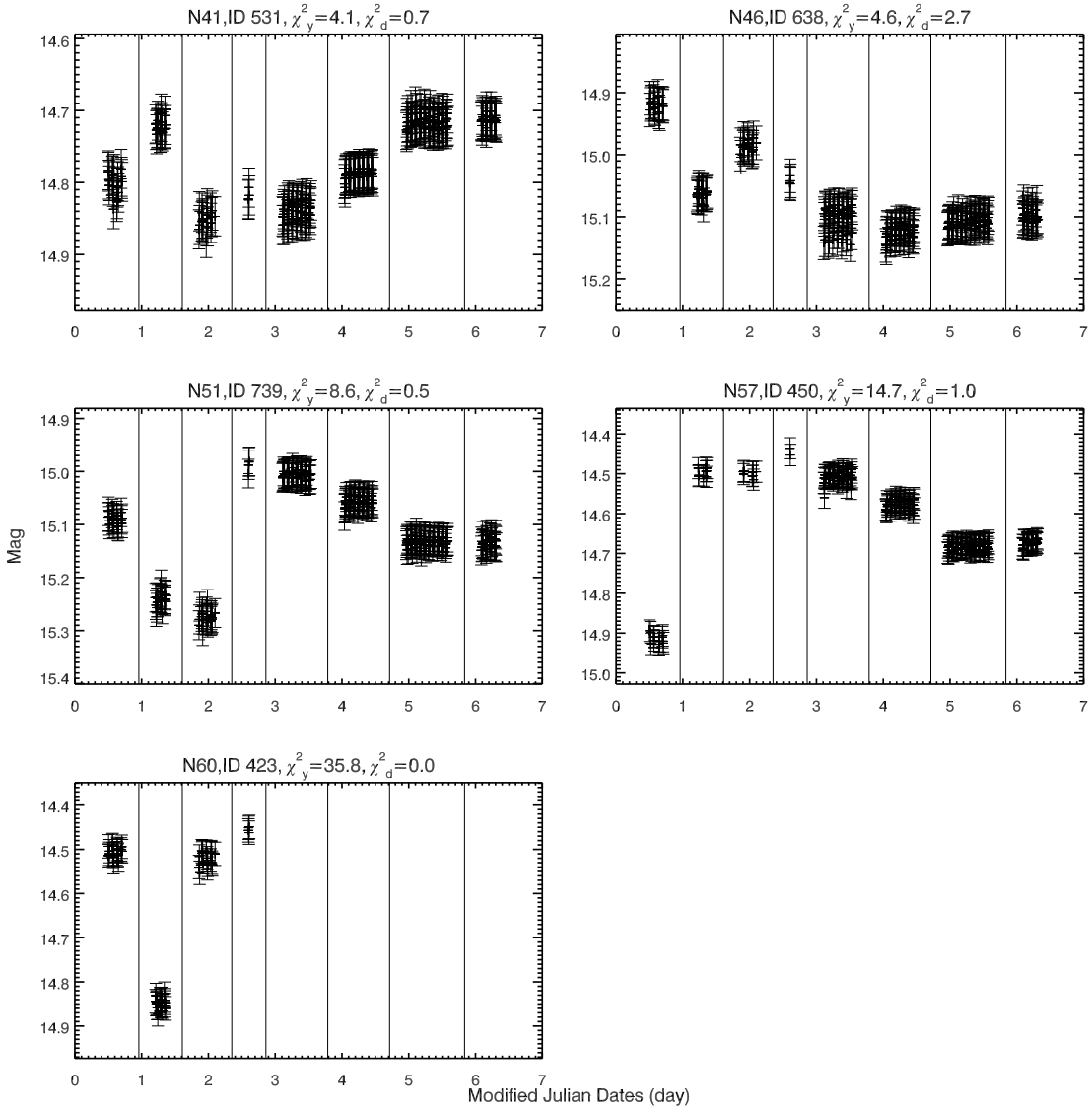

Fig. 22.— The *HST*/WFC3 F153M light curves of five CCEP candidates, which are classified as intermediate-age stars (50 to 500 Myr old) by Nishiyama et al. (2016) and show variability among years. The symbols ('pluses' and vertical lines) are the same as those in Fig. 7. In the title of each figure, we give the ID Nishiyama et al. (2016), which begins with 'N', our source ID, χ^2_y and χ^2_d, as defined in §3. ID 423 ('N60') is near the edge of our FoV and was only covered by the observations earlier than Feb 28, 2014.

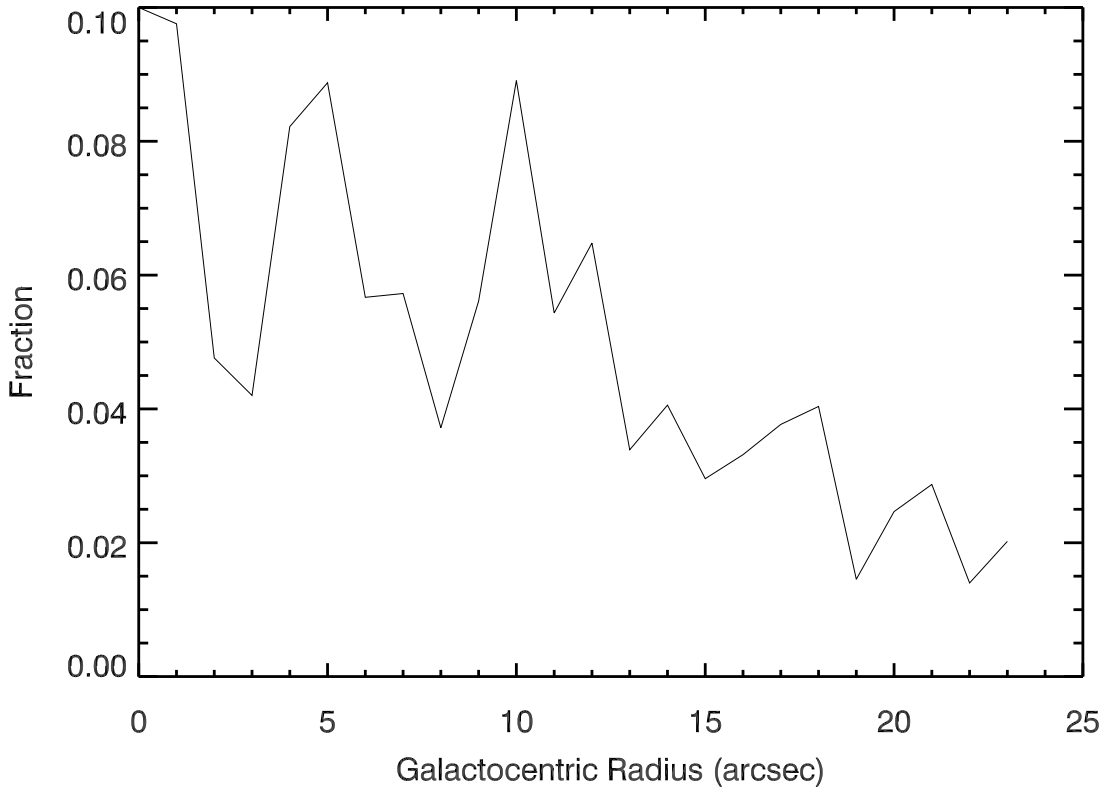

Fig. 23.— The fraction of sources, which have counterparts less than 0.13″ away, less than 2.5 mag difference at the K-band and relative proper motion > 127 km s^{-1} as a function of galactocentric radius away from Sgr A*, derived from the information given in Schödel et al. (2009).

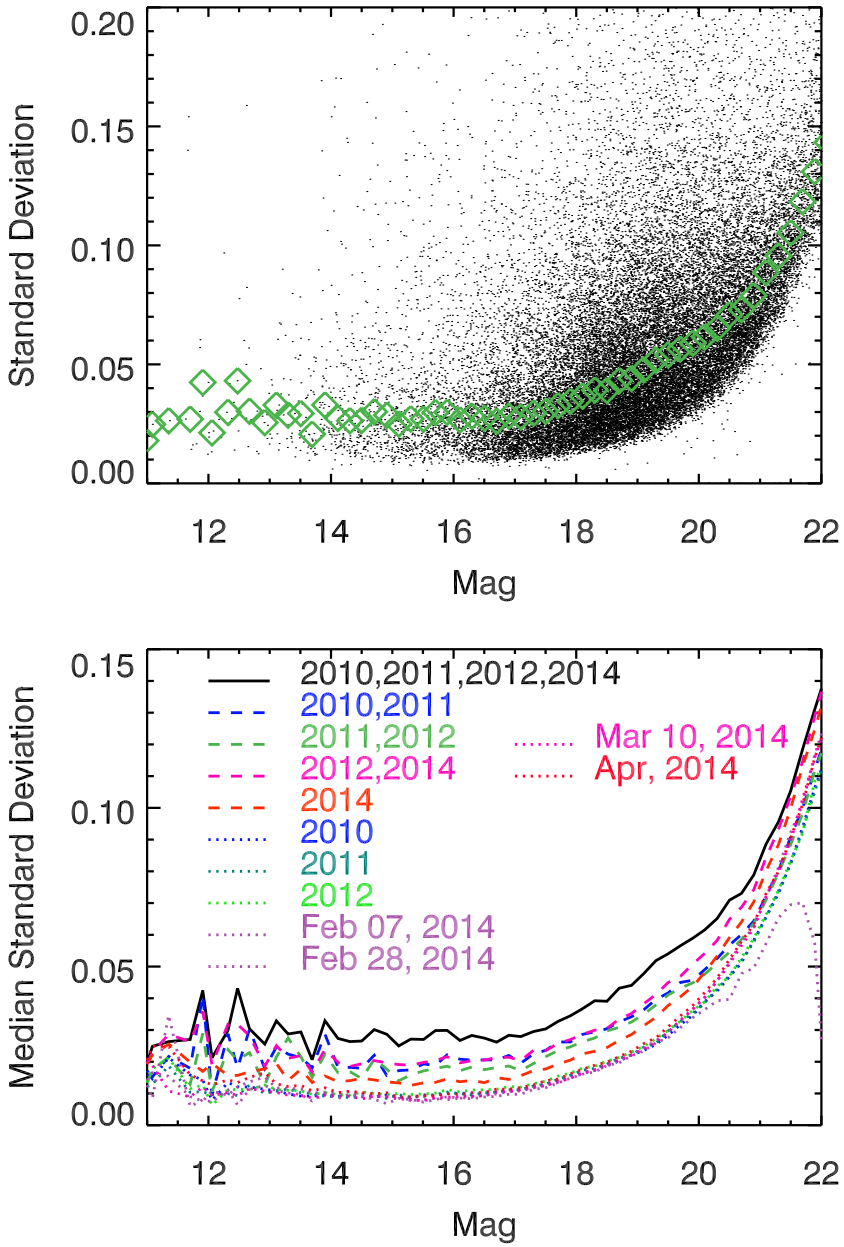

Fig. 24.— Top panel: black dots represent the standard deviation of magnitudes from 290 dithered exposures for individual sources as a function of their F153M magnitude. For each 0.03 mag, we calculate the median value of the standard deviation (green diamonds). Bottom panel, the lines with different colours and styles show the median standard deviations of magnitudes from dithered exposures at different periods as a function of F153M magnitude.

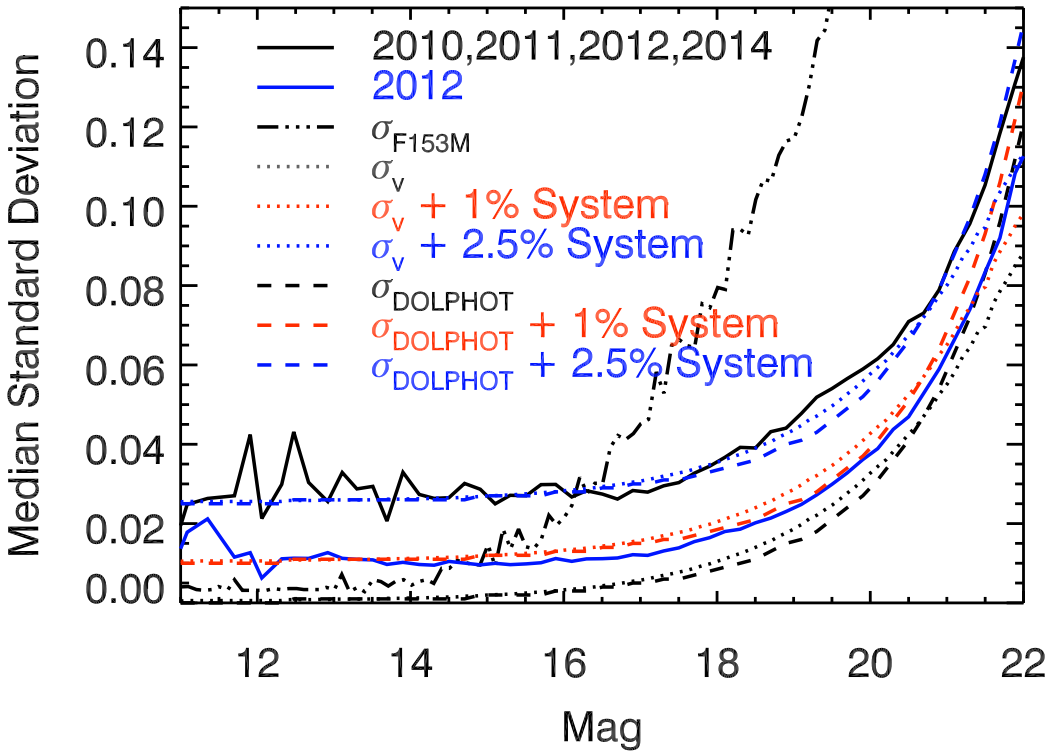

Fig. 25.— Compare the median standard deviations of magnitudes from the real observations (solid lines) and those from the artificial star tests (dotted lines and a dot dashed line) and the DOLPHOT (dashed lines).

REFERENCES

Alcock, C., Allsman, R. A., Alves, D. R., et al. 1999, AJ, 117, 920

Becker, S. A., Iben, I., Jr., & Tuggle, R. S. 1977, ApJ, 218, 633

Bartko, H., Martins, F., Fritz, T. K., et al. 2009, ApJ, 697, 1741

Blum, R. D., Ramírez, S. V., Sellgren, K., & Olsen, K. 2003, ApJ, 597, 323

Blum, R. D., Sellgren, K., & Depoy, D. L. 1996, ApJ, 470, 864

Boehle, A., Ghez, A. M., Schödel, R., et al. 2016, ApJ, 830, 17

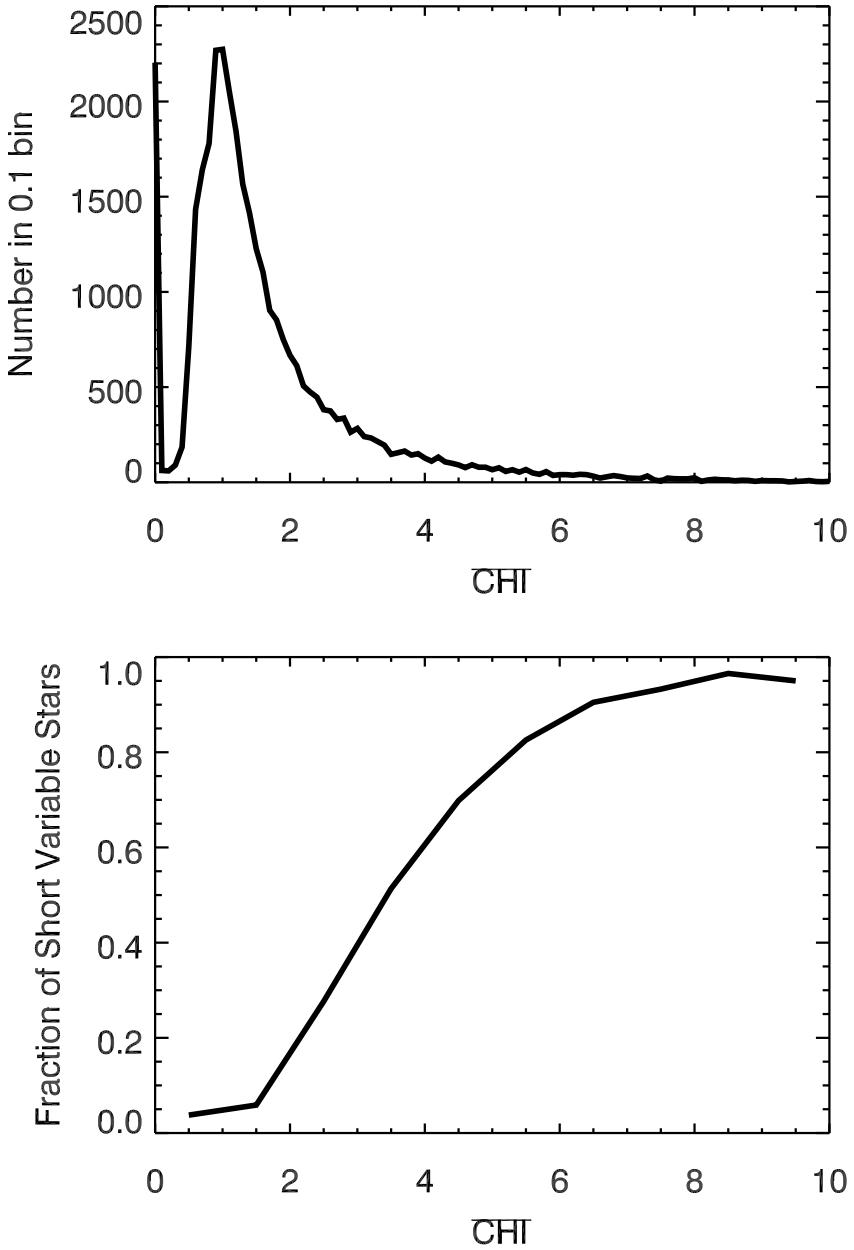

Fig. 26.— Tope panel: the mean 'CHI' ($\overline{CHI}$) distribution of dithered exposures from Groups 5 to 7 in Table1 for individual sources. Bottom panel: the fraction of sources with $\chi^2_d > 2.42$ as a function of $\overline{CHI}$.

Carr, J. S., Sellgren, K., & Balachandran, S. C. 2000, ApJ, 530, 307

Castelli, F., & Kurucz, R. L. 2004, arXiv:astro-ph/0405087

Catelan, M., Pritzl, B. J., & Smith, H. A. 2004, ApJS, 154, 633

Catelan, M. 2009, Ap&SS, 320, 261

Chatzopoulos, S., Fritz, T. K., Gerhard, O., et al. 2015, MNRAS, 447, 948

Crowther, P. A. 2007, ARA&A, 45, 177

Dalcanton, J. J., Williams, B. F., Lang, D., et al. 2012a, ApJS, 200, 18

Dalcanton, J. J., Williams, B. F., Melbourne, J. L., et al. 2012b, ApJS, 198, 6

Dahlen, T. 2013, Space Telescope WFC Instrument Science Report,

Deguchi, S., Imai, H., Fujii, T., et al. 2004, PASJ, 56, 261

Do, T., Ghez, A. M., Morris, M. R., et al. 2009, ApJ, 703, 1323

Do, T., Lu, J. R., Ghez, A. M., et al. 2013, ApJ, 764, 154

Do, T., Kerzendorf, W., Winsor, N., et al. 2015, ApJ, 809, 143

Dolphin, A. E. 2000, PASP, 112, 1383

Dong, H., Wang, Q. D., Cotera, A., et al. 2011, MNRAS, 417, 114

Dong, H., Wang, Q. D., & Morris, M. R. 2012, MNRAS, 425, 884

Dong, H., Schodel, R., Williams, B. F., et al. 2017, arXiv:1706.03299

Feast, M. W., Glass, I. S., Whitelock, P. A., & Catchpole, R. M. 1989, MNRAS, 241, 375

Feldmeier-Krause, A., Neumayer, N., Schödel, R., et al. 2015, A&A, 584, A2

Feldmeier-Krause, A., Kerzendorf, W., Neumayer, N., et al. 2017, MNRAS, 464, 194

Figer, D. F., McLean, I. S., & Morris, M. 1999, ApJ, 514, 202

Figer, D. F., Najarro, F., Gilmore, D., et al. 2002, ApJ, 581, 258

Figer, D. F., Rich, R. M., Kim, S. S., Morris, M., & Serabyn, E. 2004, ApJ, 601, 319

Fiorentino, G., Caputo, F., Marconi, M., & Musella, I. 2002, ApJ, 576, 402

Genzel, R., Schödel, R., Ott, T., et al. 2003, ApJ, 594, 812

Ghez, A. M., Salim, S., Weinberg, N. N., et al. 2008, ApJ, 689, 1044-1062

Gillessen, S., Eisenhauer, F., Fritz, T. K., et al. 2009, ApJ, 707, L114

Gillessen, S., Genzel, R., Fritz, T. K., et al. 2012, Nature, 481, 51

Glass, I. S., & Lloyd Evans, T. 1981, Nature, 291, 303

Glass, I. S., Matsumoto, S., Carter, B. S., & Sekiguchi, K. 2001, MNRAS, 321, 77

Gray, M. D., Wittkowski, M., Scholz, M., et al. 2009, MNRAS, 394, 51

Haller, J. W., & Rieke, M. J. 1989, The Center of the Galaxy, 136, 487

Hornstein, S. D., Ghez, A. M., Tanner, A., et al. 2002, ApJ, 577, L9

Hosek, M. W., Jr., Lu, J. R., Anderson, J., et al. 2015, ApJ, 813, 27

Ita, Y., Tanabé, T., Matsunaga, N., et al. 2004, MNRAS, 347, 720

Kiss, L. L., Szabó, G. M., & Bedding, T. R. 2006, MNRAS, 372, 1721

Klagyivik, P., & Szabados, L. 2009, A&A, 504, 959

Lançon, A., & Wood, P. R. 2000, A&AS, 146, 217

Lee, Y.-W. 1992, AJ, 104, 1780

Lefèvre, L., Marchenko, S. V., Moffat, A. F. J., & Acker, A. 2009, A&A, 507, 1141

Lomb, N. R. 1976, Ap&SS, 39, 447

Lu, J. R., Do, T., Ghez, A. M., et al. 2013, ApJ, 764, 155

McNamara, D. H., Clementini, G., & Marconi, M. 2007, AJ, 133, 2752

Marconi, M., Coppola, G., Bono, G., et al. 2015, ApJ, 808, 50

Maness, H., Martins, F., Trippe, S., et al. 2007, ApJ, 669, 1024

Matsunaga, N., Fukushi, H., Nakada, Y., et al. 2006, MNRAS, 370, 1979

Matsunaga, N., Kawadu, T., Nishiyama, S., et al. 2009, MNRAS, 399, 1709

Matsunaga, N., Kawadu, T., Nishiyama, S., et al. 2011, Nature, 477, 188

Matsunaga, N., Feast, M. W., Kawadu, T., et al. 2013, MNRAS, 429, 385

Matsunaga, N., Fukue, K., Yamamoto, R., et al. 2015, ApJ, 799, 46

Mossoux, E., Grosso, N., Bushouse, H., et al. 2016, A&A, 589, A116

Nagayama, T., Nagashima, C., Nakajima, Y., et al. 2003, Proc. SPIE, 4841, 459

Nishiyama, S., Tamura, M., Hatano, H., et al. 2009, ApJ, 696, 1407

Nishiyama, S., Schödel, R., Yoshikawa, T., et al. 2016, A&A, 588, A49

Ott, T., Eckart, A., & Genzel, R. 1999, ApJ, 523, 248

Paumard, T., Genzel, R., Martins, F., et al. 2006, ApJ, 643, 1011

Pavlovsky, C., McCullough, P., & Baggett, S. 2011, Space Telescope WFC Instrument Science Report,

Pawlak, M., Soszyński, I., Pietrukowicz, P., et al. 2014, Acta Astron., 64, 293

Peeples, M. S., Stanek, K. Z., & Depoy, D. L. 2007, Acta Astron., 57, 173

Reid, M. J., Menten, K. M., Trippe, S., Ott, T., & Genzel, R. 2007, ApJ, 659, 378

Pfuhl, O., Fritz, T. K., Zilka, M., et al. 2011, ApJ, 741, 108

Pfuhl, O., Alexander, T., Gillessen, S., et al. 2014, ApJ, 782, 101

Poleski, R., Soszyński, I., Udalski, A., et al. 2010, Acta Astron., 60, 1

Rafelski, M., Ghez, A. M., Hornstein, S. D., Lu, J. R., & Morris, M. 2007, ApJ, 659, 1241

Sandage, A., & Tammann, G. A. 2006, ARA&A, 44, 93

Scargle, J. D. 1982, ApJ, 263, 835

Schödel, R., Eckart, A., Alexander, T., et al. 2007, A&A, 469, 125

Schödel, R., Merritt, D., & Eckart, A. 2009, A&A, 502, 91

Schödel, R., Najarro, F., Muzic, K., & Eckart, A. 2010, A&A, 511, A18

Schödel, R. 2010, A&A, 509, A58

Scoville, N. Z., Stolovy, S. R., Rieke, M., Christopher, M., & Yusef-Zadeh, F. 2003, ApJ, 594, 294

Soszynski, I., Udalski, A., Kubiak, M., et al. 2004, Acta Astron., 54, 129

Soszyński, I., Udalski, A., Szymański, M. K., et al. 2008, Acta Astron., 58, 293

Soszyński, I., Udalski, A., Pietrukowicz, P., et al. 2011, Acta Astron., 61, 285

Soszyński, I., Wood, P. R., & Udalski, A. 2013, ApJ, 779, 167

Soszyński, I., & Udalski, A. 2014, ApJ, 788, 13

Støstad, M., Do, T., Murray, N., et al. 2015, ApJ, 808, 106

Tamura, M., Werner, M. W., Becklin, E. E., & Phinney, E. S. 1996, ApJ, 467, 645

Turner, D. G. 1996, JRASC, 90, 82

Verheyen, L., Messineo, M., & Menten, K. M. 2012, A&A, 541, A36

Wallerstein, G. 2002, PASP, 114, 689

Walker, A. R. 1989, PASP, 101, 570

Walker, A. R., & Terndrup, D. M. 1991, ApJ, 378, 119

Whitelock, P. A., Feast, M. W., & van Leeuwen, F. 2008, MNRAS, 386, 313

Williams, B. F., Lang, D., Dalcanton, J. J., et al. 2014, ApJS, 215, 9

Wood, P. R., Alcock, C., Allsman, R. A., et al. 1999, Asymptotic Giant Branch Stars, 191, 151

Wood, P. R. 2000, PASA, 17, 18

Table 1. *HST*/WFC3 observations of the central 2.3′× 2.3′ of the GC

Group ID	Observation Date (GMT)	Program	Duration (hours)	Number of Pointings	Number of Dithered Exposures	Exposure Time (s)
F153M Observations						
1	2010-06-29	GO-11671	5	1	21	7334
2	2011-09-08	GO-12318	3.5	1	21	7334
3	2012-08-09	GO-12667	6	1	21	7334
4	2014-02-07	GO-13049	0.3	1	4	997
5	2014-02-28	GO-13316/13403	10	14	56	10806
6	2014-03-10	GO-13316	10	14	55	16517
7a[1]	2014-04-02	GO-13316	15	20	80	24035
7b[1]	2014-04-03	GO-13316	5.5	8	32	9954
F127M Observations						
1	2010-08-17	GO-11671	4	1	12	7191
2	2011-05-20/21	GO-12182	0.5	8	4	1797

Note. — 1) The first dithered exposure in the group 7b was started 15.25 hours after the end of the last dithered exposure in the group 7a. Therefore, we analyzed these two groups together when we identified stars with short periods of days in §4, although we separated them when we plotted the light curves.

Table 2. Detection Limit

Area ID[a]	Size arcsec^2	Surface Brightness ergs s^{-1} cm^{-2} Å^{-1} arcsec^{-2}	Input/Output Number[b]	90% Detection Limit	50% Detection Limit
1	406	5.1×10^{-18}	63230/ 36642	21.1	22.5
2	2396	8.1×10^{-18}	499053/ 214436	19.8	21.5
3	4294	12.7×10^{-18}	1488127/ 462869	19.0	20.7
4	5607	20.1×10^{-18}	2723407/ 585244	18.3	20.0
5	3790	31.8×10^{-18}	2351949/ 337882	17.5	19.2
6	1593	50.1×10^{-18}	1182158/ 108677	16.7	18.5
7	529	79.1×10^{-18}	463717/ 27890	15.6	17.9
8	148	124.9×10^{-18}	136886/ 4448	15.1	17.1
9	28	197.1×10^{-18}	26316/ 453	14.2	16.4
10	8	311.1×10^{-18}	8549/ 87	14.1	15.8

Note. — [a] The larger the 'Area ID' is, the higher the surface brightness is; [b] 'Input/Ouput Number' means the numbers of artificial stars inserted into each annulus and then recovered by the 'DOLPHOT' package.

Table 3. Source Catalog

ID	RA	Dec	F153M[a]	σ_{F153M}[b]	F127M[a]	σ_{F127M}[b]	χ^2_y	$\chi^2_{y,b}$	χ^2_d	$\chi^2_{d,b}$	V?[c]
1	266.40831	-29.02624	1.00	+0.004±0.001	1.00	+9.900±9.900	2.0	0.3	11.5	0.6	0
2	266.40634	-29.02650	10.38	+0.004±0.000	11.32	+0.003±0.000	0.9	0.1	6.6	0.2	0
3	266.42049	-29.02490	10.51	+0.004±0.001	11.00	+0.003±0.000	0.7	0.1	5.5	0.2	0
4	266.41602	-29.01495	10.66	+0.004±0.001	13.28	+0.003±0.001	1.6	0.7	7.9	0.1	0
5	266.41749	-29.01606	10.98	+0.004±0.011	12.86	+0.003±0.000	0.5	0.1	3.9	0.2	0
6	266.39496	-29.01075	11.09	+0.004±0.015	11.72	+0.003±0.001	0.9	0.2	5.5	0.2	0
7	266.43080	-29.00743	11.34	+0.004±0.017	12.03	+0.003±0.001	0.7	0.1	4.4	0.1	0
8	266.42854	-28.99368	11.37	+0.004±0.018	12.06	+0.003±0.001	1.0	0.2	5.2	0.0	0
9	266.42271	-28.99041	11.62	+0.004±0.006	13.83	+0.003±0.001	1.1	0.5	3.4	0.1	0
10	266.41685	-29.00629	11.66	+0.004±0.019	15.65	+0.004±0.002	29.2	22.5	1.4	0.1	1
...	...	...	...	...	...	...	...	...	...	...	...

Note. — The complete source list will be published online. The sources have been sorted according to their mean magnitudes. [a] If the source is saturated, its magnitude is 1; If the source is undetected, its magnitude is 99; [b] the first and the second values are the systematic and statistic uncertainties determined from the artificial star tests (see §2.2). Because of the confusion, the output magnitude is smaller than the input magnitude. Therefore, the systematic uncertainty is positive; [c] **The index which shows whether the source is variable or not:** '0', '1', '2', '3' means non-variable, stars varying on yearly time scales, stars with intraday variability and stars varying on both yearly and daily time scales, respectively.

Table 4. Magnitudes in Individual Dithered Exposures

ID	Julian Date(day)	Mag[a]	σ_v	S/N	Sharp[2]	Crowd	Flag
...	...	...	...	...	...	...	..
3	55376.295	10.54	0.015	4142.3	0.0003	0.016	4
3	55376.300	10.54	0.015	4341.9	0.0002	0.014	4
3	55376.305	10.51	0.015	5536.4	0.0010	0.007	0
3	55376.310	10.53	0.015	4163.1	0.0011	0.014	4
3	55376.314	10.53	0.015	4416.6	0.0007	0.015	4
3	55376.357	10.53	0.015	4214.7	0.0003	0.017	4
3	55376.362	10.52	0.015	5531.3	0.0007	0.009	0
3	55376.367	10.51	0.015	5544.4	0.0007	0.008	0
3	55376.371	10.52	0.015	5524.5	0.0020	0.009	0
3	55376.376	10.52	0.015	5537.4	0.0025	0.010	0
...	...	...	...	...	...	...	..

Note. — The complete source list will be published online. [a] If the source is saturated, its magnitude is 1; If the source is undetected, its magnitude is 99.

Table 5. Statistic values of χ^2_y and χ^2_d

	Median	68% percentile	90% percentile
χ^2_y	0.94	[0.41,3.04]	[0.23,8.21]
$\chi^2_{y,b}$	0.56	[0.19,2.49]	[0.09,8.21]
χ^2_d	1.00	[0.58,2.42]	[0.42,6.44]
$\chi^2_{d,b}$	0.30	[0.14,0.59]	[0.09,0.83]

Table 6. Periods

ID	Period	F153M	F127M-F153M
2495	0.542	16.6	0.6
6164	0.195	17.7	2.0
7831	0.299	18.0	2.6
8735	0.559	18.1	2.2
9074	0.838	18.2	2.0
10520	0.542	18.4	1.9
12097	0.489	18.6	2.7
12215	0.089	18.6	2.0
13950	0.686	18.8	2.4
14123	0.384	18.8	2.5
14583	0.677	18.9	2.4
15242	0.329	18.9	1.8
19440	0.294	19.5	2.0
20785	0.171	19.6	1.8
20993	0.368	19.7	2.0
21740	0.244	19.8	2.3
22081	0.495	19.8	2.6
22197	0.593	19.8	2.9
22312	0.573	19.9	2.5
23037	0.469	20.0	2.3
23523	1.103	20.0	2.6
23605	1.142	20.0	3.1
25542	0.258	20.3	1.9
25912	0.644	20.4	3.3
26112	1.299	20.4	2.8
26822	0.722	20.5	2.3
28701	0.235	20.9	1.8
29285	0.168	21.0	1.7
1365	2.279	15.9	2.7
1404	1.565	15.9	0.5
2980	0.584	16.8	1.3
10110	2.005	18.3	2.2
21377	2.016	19.7	1.9

Table 6—Continued

ID	Period	F153M	F127M-F153M
21717	0.814	19.8	2.0
27035	2.320	20.6	2.9
27972	1.439	20.7	2.4

Note. — The lightcurves of the first 28 sources are shown in Figs. 12 to 14, while the last 8 sources are given in Fig. 15.

Table 7. Previous Variability Studies

References[a]	Instruments	FoV	Time Range	Identified Variables[b]	Recovered
(1)	Steward 1.54m	$5'\times5'$	1986-1988	12 without astrometry	
(2)	IRTF 3m	$\sim23''\times23''$	1991-1993	6	6
(3)	CTIO 4m/OSIRIS	$2'\times2'$	1993, 1995	3	3
(4)	NTT 3.6m/SHARP I	$20''\times20''$	1992-1998	108 (112)	48
(5)	SAAO 0.75m/PANIC	$24'\times24'$	1994-1997	10 (409)	7
(6)	CTIO Yalo 1m/ANDICAM	$112''\times112''$	2000-2002	8(112)	2
(7)	VLBA/VLA		1995-2006	12(15)	11
(8)	Keck 10m/NIRC	$5''\times5''$	1995-2004	10(15)	3
(9)	IRSF 1.4m/SIRIUS	$20'\times20'$	2001-2008	17/(1364)	15
(10)	VLT 8m/NAOC/SINFONI	$20''\times20''$	2003-2013	2	1

Note. — [a] (1) Haller & Rieke (1989); (2) Tamura et al. (1996); (3) Blum et al. (1996); (4) Ott et al. (1999); (5) Glass et al. (2001); (6) Peeples et al. (2007); (7) Reid et al. (2007); (8) Rafelski et al. (2007); (9) Matsunaga et al. (2009, 2011, 2013); (10) Pfuhl et al. (2014). [b] the first values are the numbers of variables, which have counterparts in our source catalog, while the values in the parentheses are the original numbers of variable stars,

Table 8. Cross Correlations With Previous Variability Study

ID	(1)	(2)	(3)	(4)	(5)	(6)	(7)	(8)	(9)
1					PSDJ174537.98-290134.4				
4					PSDJ174539.83-290053.9				
10	IRS7	IRS7	1		PSDJ174540.04-290022.7	IRS7			
11				3-5	PSDJ174542.72-285957.4	SiO6		680	
14			2		PSDJ174540.25-290027.2		IRS16NE		IRS16NE
15					PSDJ174536.63-290015.4				
17					PSDJ174543.01-290011.9				
20					PSDJ174542.39-285950.7				
25					PSDJ174538.74-290012.7				
26					PSDJ174541.17-290046.9				
...	...	...	...	...	...	...	...	...	..

Note. — References: (1) Tamura et al. (1996); (2) Blum et al. (1996); (3) Ott et al. (1999) ('ID' column in its Table 2); (4) Glass et al. (2001) ('Iden.' column in its Table 2); (5) Peeples et al. (2007) ('ID' column in its Tables 1 and 2); (6) Reid et al. (2007) ('Star' column in its Table 1); (7) Rafelski et al. (2007) ('Star ID' column in its Tables 2 and 3); (8) Matsunaga et al. (2009) ('No.' column in its Table 6); (9) Pfuhl et al. (2014). The complete lists will be published online.

Table 9. Cross Correlations With Previous Spectroscopy Study

ID	Name	(1)	(2)	(3)	(4)	(5)	(6)	(7)	(8)	(9)
10	IRS7	66(I)								25352(Late)
11	IRS24	128(LPV)								
27	IRS17	105(LPV?)								25351(Late)
31	IRS23	136(LPV?)								
38		11(III)								
39		140(III)								
42	IRS9	91(LPV)								25348(Late)
43	IRS16SW	71(24000)		E23(Ofpe/WN9)	9(Early)	S1-34(l)		97(Ofpe/WN9)		
70	IRS14SW	60()								1(Late)
71		126(III)								
...	...	...	...	...	...	...	...	...	..	

Note. — References: (1) Blum et al. (2003); (2) Maness et al. (2007); (3) Paumard et al. (2006); (4) Bartko et al. (2009); (5) Do et al. (2013); (6) Støstad et al. (2015); (7) Feldmeier-Krause et al. (2015); (8) Nishiyama et al. (2016); (9) Feldmeier-Krause et al. (2017). The complete lists will be published online.

Table 10. Type II Cepheid Candidates

ID	$A^{a}_{Ks,CCEPs}$	Dis^{a}_{CCEPs}	$A^{b}_{Ks,T2Cs}$	Dis^{b}_{T2Cs}
23523	2.47±0.12	28.0±2.70	2.43±0.12	15.6±2.50
23605	2.86±0.17	18.8±2.74	2.88±0.17	10.4±2.52
26112	2.54±0.16	32.9±3.54	2.57±0.16	17.7±3.27

Note. — ^{a}, **the values were determined** with the assumption of the PL relationship for CCEPs given in Matsunaga et al. (2013) and distances in units of kpc. ^{b}, **the values were determined** with the assumption of the PL relationship for T2Cs given in Matsunaga et al. (2013) and distances in units of kpc.